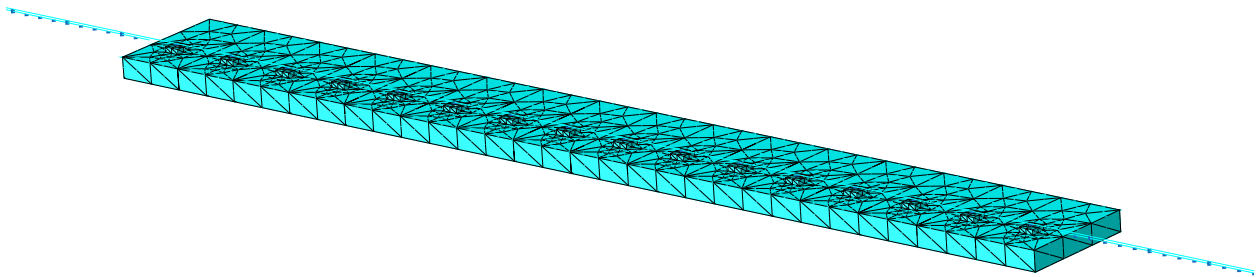




CHALMERS
UNIVERSITY OF TECHNOLOGY



A Parameterized Three-Dimensional Finite Element Model of a Slab Track for Simulation of Dynamic Vehicle–Track Interaction

Master's thesis in Structural Engineering and Building Technology

NIKLAS SVED

Department of Mechanics and Maritime Sciences
CHALMERS UNIVERSITY OF TECHNOLOGY
Gothenburg, Sweden 2018

MASTER'S THESIS 2018:01

**A parameterized three-dimensional finite element
model of a slab track for simulation of dynamic
vehicle–track interaction**

NIKLAS SVED



CHALMERS
UNIVERSITY OF TECHNOLOGY

Department of Mechanics and Maritime Sciences

Division of Dynamics

CHALMERS UNIVERSITY OF TECHNOLOGY

Gothenburg, Sweden 2018

A parameterized three-dimensional finite element model of a slab track for simulation
of dynamic vehicle–track interaction
NIKLAS SVED

© NIKLAS SVED, 2018.

Supervisors: Emil Aggestam and Peter Torstensson, Department of Mechanics and
Maritime Sciences

Examiner: Jens Nielsen, Department of Mechanics and Maritime Sciences

Master's Thesis 2018:01

Department of Mechanics and Maritime Sciences

Division of Dynamics

Chalmers University of Technology

SE-412 96 Gothenburg

Telephone +46 31 772 1000

Cover: Three-dimensional finite element model of a slab track structure generated
in the commercial software ABAQUS.

Gothenburg, Sweden 2018

A parameterized three-dimensional finite element model of a slab track for simulation of dynamic vehicle–track interaction

NIKLAS SVED

Department of Mechanics and Maritime Sciences

Chalmers University of Technology

Abstract

To meet the increased demands of freight and people transport by trains, the Swedish Transport Administration is evaluating the possibility of constructing new railways based on slab track design. In this work, models of a slab track have been developed in two and three spatial dimensions. The models were created by writing scripts in the programming language Python and by generating models in the commercial software ABAQUS. The models were subsequently used in dynamic vehicle–track interaction simulations in the in-house software DIFF. The two-dimensional slab track model consists of Rayleigh–Timoshenko beam elements, while the three-dimensional slab track model combines Rayleigh–Timoshenko beams and solid elements. All track parameters, geometries, materials and the foundation stiffness distribution are modifiable such that parametric studies can be conducted.

Track models developed within the current project have been validated against an existing two-dimensional track model, in terms of receptance, track stiffness at the rail level and wheel–rail contact force. These numerical results give an indication if the assumptions for the existing two-dimensional model are valid, they also offer an opportunity to fine-tune said existing two-dimensional model according to a more detailed three-dimensional model in future work. The results in the current work indicate that the three-dimensional model is slightly stiffer. However, by tuning the design parameters, a similar track stiffness at the rail level can be achieved.

Keywords: Vehicle–track interaction; Slab track; Ballastless track; Modeling; ABAQUS scripting.

En parameteriserad tredimensionell finita element modell av ett fixerat tågspår för simulering av dynamisk fordon–spårinteraktion

NIKLAS SVED

Institutionen för mekanik och maritima vetenskaper

Chalmers tekniska högskola

Sammanfattning

För att möta den ökade efterfrågan av spårburen gods- och persontrafik utreder Trafikverket förutsättningarna för nya stambanor byggda med fixerat (ballastfritt) spår. I detta arbete har modeller av ett fixerat spår i två och tre rumsdimensioner tagits fram med hjälp av finita elementmetoden. Modellerna skapades genom att skriva kod i programmeringsspråket Python, samt genom att generera modeller i den kommersiella mjukvaran ABAQUS. Modellerna användes sedan i simuleringar av dynamisk tåg–spårinteraktion i det interna programmet DIFF. Den tvådimensionella spårmodellen består av Rayleigh–Timoshenko balkelement, medan den tredimensionella spårmodellen består av Rayleigh–Timoshenko balkelement samt solida element. Alla spårparametrar, geometri, material samt fördelning av markstyvhet är modifierbara så att parameterstudier kan genomföras.

Båda spårmodellerna utvecklade i detta projekt har validerats mot en existerande modell med hänsyn till receptans, spårstyvhet på rälnivån samt hjul–räl kontaktkrafter. Dessa numeriska resultat ger en indikation huruvida antagelserna för den existerande tvådimensionella modellen är godtagbara, de ger även en möjlighet att finjustera den befintliga tvådimensionella modellen mot en mer detaljerad tredimensionell modell i vidare arbete. Resultaten i detta projekt indikerar att den tredimensionella modellen är något styvare. Genom att justera designparametrarna kan en liknande styvhet på rälnivån uppnås.

Nyckelord: Fordon–spårinteraktion; Fixerat spår; Modeller; Ballastfritt spår; ABAQUS skriptning.

Preface

This thesis was carried out during the period of August 2017 to January 2018 as the finishing work to complete my master's degree within Structural Engineering and Building Technology at Chalmers University of Technology. The work was carried out at the Division of Dynamics at the Department of Mechanics and Maritime Sciences at Chalmers University of Technology in Gothenburg. The work was supervised by Mr. Emil Aggestam and Dr. Peter Torstensson and the examiner was Prof. Jens Nielsen, all at the Division of Dynamics.

Special gratitude goes to my supervisors Emil and Peter for always being there when I needed it. Your help and guiding input were vital components to complete this work. Furthermore, a big thank you goes out to Roeland Bisschop, Michele Maglio, Carolyn Oddy and Thomas van Westendorp for being yourselves. Hanging out with you for coffee, lunch and outside school hours kept me going to complete this work.

Niklas Sved, Gothenburg, January 2018

Nomenclature

Complex quantities are indicated with underbars and local spatial coordinates are marked with overbars. Dots over variables indicate time derivative and superscripts t and v denote track and vehicle respectively. Superscript T denotes the transpose of a matrix or vector.

Abbreviations

API	Application programming interface
DOF	Degree of freedom
E–B	Euler-Bernoulli
FE	Finite element
FEM	Finite element method
FPL	Frost protection layer
HBL	Hydraulically bound layer
MPC	Multi-Point Constraint
R–T	Rayleigh-Timoshenko

Variables

A	Area [m ²]
a	Contact radius [m]
\mathbf{C}	Global viscous damping matrix $\left[\frac{\text{Ns}}{\text{m}}\right]$, [Ns], [Nms]
c_f	Foundation damping $\left[\frac{\text{Ns}}{\text{m}^2}\right]$, $\left[\frac{\text{Ns}}{\text{m}^3}\right]$
C_H	Hertzian constant $\left[\frac{\text{N}}{\text{m}^{\frac{3}{2}}}\right]$
c_p	Rail pad damping $\left[\frac{\text{Ns}}{\text{m}}\right]$
Δ	Deflection [m]
E	Young's modulus $\left[\frac{\text{N}}{\text{m}^2}\right]$
ε	Strain [-]
EI	Bending stiffness [Nm ²]
G	Shear modulus $\left[\frac{\text{N}}{\text{m}^2}\right]$
γ	Shearing angle [-]
$\underline{H}^t(\omega)$	Receptance $\left[\frac{\text{m}}{\text{N}}\right]$

I	Area moment of inertia [m ⁴]
\mathbf{K}	Global stiffness matrix $\left[\frac{\text{N}}{\text{m}}\right], [\text{N}], [\text{Nm}]$
k'	Timoshenko shear coefficient [-]
k_f	Foundation stiffness $\left[\frac{\text{N}}{\text{m}^2}\right], \left[\frac{\text{N}}{\text{m}^3}\right]$
k_H	Hertzian contact stiffness $\left[\frac{\text{N}}{\text{m}}\right]$
k_p	Rail pad stiffness $\left[\frac{\text{N}}{\text{m}}\right]$
l_b	Rail seat distance [m]
l_j	Length of a beam element [m]
l_s	Length of the solid part of the 3D slab track model [m]
l_t	Track length [m]
M	Bending moment [Nm]
\mathbf{M}	Mass matrix [kg], [kgm ²]
N	Wheel–rail normal contact force [N]
ν	Poisson's ratio [-]
ω_n	Angular eigenfrequency number n $\left[\frac{1}{\text{s}}\right]$
P	Nodal force [N]
ψ	Bending angle [-]
$\underline{\mathbf{P}}$	Modal matrix $[-], \left[\frac{1}{\text{m}}\right]$
p_f	Force on elastic foundation $\left[\frac{\text{N}}{\text{m}}\right]$
p_y	Continuous transverse force $\left[\frac{\text{N}}{\text{m}}\right]$
$\underline{\mathbf{Q}}^t(t)$	Modal load vector [N]
$\underline{\mathbf{q}}^t(t)$	Modal displacement vector [m]
R	Radius [m]
ρ	Density $\left[\frac{\text{kg}}{\text{m}^3}\right]$
$\underline{\boldsymbol{\rho}}^{(n)}$	Eigenvector $\left[\frac{1}{\text{m}}\right]$
S	Shear force [N]
σ	Normal stress $\left[\frac{\text{N}}{\text{m}^2}\right]$
u	Displacement [m]
v	Vehicle speed $\left[\frac{\text{m}}{\text{s}}\right]$
w	Transverse deflection [m]
$\bar{x}, \bar{y}, \bar{z}$	Local spatial variables [m]
\mathbf{x}^{irr}	Irregularity vector [m]
$\underline{F}_r^t(\omega)$	Reaction force at the rail [m]
$\underline{F}_s^t(\omega)$	Reaction force at the slab [m]
$\underline{x}_r^t(\omega)$	Displacement at the rail [m]
$\underline{x}_s^t(\omega)$	Displacement at the slab [m]
x, y, z	Global spatial variables [m]

Contents

Abstract	i
Sammanfattning	ii
Preface	iii
Nomenclature	v
List of Figures	ix
List of Tables	xv
1 Introduction	1
1.1 Background	1
1.2 Aim	2
1.3 Limitations	2
1.4 Report Layout	3
2 Theory	5
2.1 Slab Tracks — Design and Historical Review	5
2.1.1 Common Designs	6
2.1.2 Typical Components	7
2.2 Historical Modeling of Track Systems	7
2.2.1 Rayleigh–Timoshenko Beam Theory	8
2.2.2 Winkler Foundation	11
2.3 Simulation of Dynamic Vehicle–Track Interaction	12
2.3.1 Normal Wheel–Rail Contact	14
2.3.2 Time-Integration of the Coupled Vehicle–Track System	16
3 Method	21
3.1 Previously Developed DIFF model	22

3.2	Implementation Phase	24
3.2.1	Two-dimensional Slab Track Model	25
3.2.2	Three-dimensional Slab Track Model	27
3.3	Simulation Phase	32
3.3.1	Non-moving Load Problem	33
3.3.2	Dynamic simulations in DIFF	34
4	Numerical Results	35
4.1	Verification of Modeling Procedure	35
4.1.1	Receptance	35
4.1.2	Track Stiffness at the Rail Level	37
4.1.3	Vertical Wheel–Rail Contact Force	38
4.2	Three-dimensional Slab Track	40
4.2.1	Receptance	40
4.2.2	Track Stiffness at the Rail Level	41
4.2.3	Vertical Wheel–Rail Contact Force	41
5	Summary and Conclusions	45
6	Further Work	47
	Bibliography	49

List of Figures

2.1	Sketch of a track profile divided into a superstructure including rails, rail pads and railway ties and a substructure including the subgrade foundation.	7
2.2	Free-body diagram of an infinitesimal part $d\bar{x}$ of a Rayleigh-Timoshenko beam in bending, where \bar{x} marks the longitudinal and \bar{y} marks the transversal direction. The beam is loaded by a transverse force $p_y(\bar{x}, t)$ and has arbitrary boundary conditions. w is the resulting transverse deflection, ψ the resulting bending angle and γ the shear angle. The model also includes the resulting internal shear force S and bending moment M . Inspired by figure 10.17 on page 718 of Benorya and Nagurka [16].	10
2.3	An infinitesimal part of a R-T beam element subjected to a transverse uniformly distributed load p_y , resting on an elastic foundation with an uniformly distributed reaction load p_f	12
2.4	Sketch of a vehicle model including the car body, bogie and wheelset. The wheelset and the bogie frame are attached to the car body via the primary and secondary suspensions.	13
2.5	Sketch of a contact between a wheel and a rail. The wheel has radii R_{x1} in the (x, y) -plane and R_{z1} (sometimes negative) in the (z, y) -plane while the rail has radii R_{z2} in the (z, y) -plane and $R_{x2} = \infty$ in the (x, y) -plane. The coordinates x, y, z are outlined. The illustration is inspired by a figure in Andersson et al. [24].	15
2.6	Sketch of the vehicle model. The model consists of one bogie, and both wheels and bogie frame are rigid bodies. x_{a1} and x_{a2} are massless DOFs in contact with the rail through springs with stiffness k_{H1} and k_{H2} respectively. DOFs x_{b1}, x_{b2} are the vertical displacements of wheelset 1 and 2, respectively, and DOFs x_{b3} and x_{b4} are the vertical displacement and pitch rotation of the bogie frame, respectively. . . .	18

3.1	Sketch of the proposed simulation procedure. First, the problem is set by determining the track design and operational conditions. In the implementation phase, the track model is parameterized in a Python script, and then generated in ABAQUS. The model is subsequently exported to Matlab for dynamic and static track simulations. Ultimately, the model can be altered based on simulation results.	21
3.2	Profile sketch of a slab track of German design with hydraulically bound layer (unreinforced roadbed in this sketch). Figure from Aggestam et al. [27].	22
3.3	Sketch of the DIFF slab track model. The model consists of two layers of beams representing the rail (r) and the concrete panel (s). The concrete panel is supported by a Winkler foundation, where the prescribed (possibly random) variation in stiffness is indicated by the irregular ground surface. Figure from Aggestam et al. [27].	23
3.4	Diagram sketch of the implementation phase in ABAQUS.	25
3.5	Sketch of a R–T 2D beam element with two nodes, each consisting of two translational and one rotational DOF. \bar{x} and \bar{y} denote the local spatial coordinates and l_j denotes the element length.	26
3.6	Magnified sketch of the 2D ABAQUS slab track model covering two rail seat distances. The upper beam layer represents the rail and the lower represents a continuous concrete slab. The rail and the slab are connected by a spring–dashpot pair at each rail seat while the slab and the ground are connected by a spring–dashpot pair at each element node as a substitute for a Winkler foundation.	27
3.7	Sketch of the foundation adapted in ABAQUS. The Winkler bed is approximated as spring/dashpot pairs coupling each node of the concrete panel to the ground represented by mass-less nodes constrained in all DOFs.	27
3.8	Sketch of the full Abaqus 2D model. Two parts are magnified; the far end illustrating the boundary conditions and the two middlemost rail seats showing the rail–panel connection. l_t is the full track length and the global coordinates, x and y are outlined.	27
3.9	Sketch of a tetrahedral element with 10 nodes with local coordinates \bar{x}, \bar{y} and \bar{z} . Each node has three translational DOFs \bar{x}_i, \bar{y}_i and \bar{z}_i where i is the node number	28

-
- 3.10 Sketch illustrating the edges arbitrating the mesh generation, which are indicated by the dashed lines in red. Input parameters decide the number of elements along each highlighted edge. 29
- 3.11 Magnified sketch of one rail seat module of the ABAQUS 3D slab track model, seen from the side (a) and from above (b). The rail and the slab are connected by a spring–dashpot pair at each rail tie connecting one rail node to all the surface nodes via the mid rail seat surface node indicated by the cross hairs on the rail seat. The slab is connected to the ground via spring–dashpot pairs with uniform stiffness and damping at each element node as a substitute for a Winkler foundation. Symmetry in the z -direction is applied in the middle of the track width. l_{bay} denotes the rail seat span length, l_{rs} is the length and width of the elevated portion of the rail seat, b_S is the concrete panel width, h_s is the concrete panel height and h_{rs} is the rail seat height. The global coordinate system is illustrated in both figures. 30
- 3.12 Sketch of different ABAQUS connection types that were verified by calculating the deflection after applying the same load P on structures with the same length l and having the same cross-sectional properties and mesh resolution. Upper left: beam with no connections. Upper right: beam to beam COUPLING connection. Lower left: Solid part with no connections. Lower right: Solid to beam MPC-beam connection. 31
- 3.13 Sketch of the MPC connection between the solid and beam element parts of the slab. The yellow nodes represent the surface nodes on the solid element, whose DOFs are all tied to the DOFs of the adjacent beam node (the red node with cross hairs). 32
- 3.14 Sketch of the whole 3D ABAQUS track model. Three sections of the model are magnified. The far end, a rail seat distance modelled with solid elements and the MPC connection between solid and beam elements. l_s denotes the length of the solid part of the track and l_t is the total length of the track. The global x , y and z coordinates are outlined. 32

3.15	In the simulation phase, the node and element information is used to sort the global system matrices exported to Matlab and subsequently used in the simulations. The simulation results include receptance, track stiffness at the rail level and wheel–rail contact forces calculated in the software DIFF.	33
4.1	Magnitude (a) and relative error (b) of the direct receptance calculated for the 2D ABAQUS model and the DIFF model. The excitation and response are taken at the middle rail seat.	36
4.2	Magnitude (a) and relative error (b) of the cross receptance calculated for the ABAQUS 2D model and the DIFF model. The excitation and response are taken at the longitudinal coordinate corresponding to the mid rail seat at the rail and slab, respectively.	36
4.3	Magnitude (a) and relative error (b) of the slab track stiffness at the rail level calculated for the 2D ABAQUS model and the previously developed DIFF model.	37
4.4	Magnitude (a) and relative error (b) of vertical wheel–rail contact force simulated using the ABAQUS 2D model and the previously developed DIFF model. Time step 10^{-5} s. Locations of rail seats and nodes of beam elements in the rail FE model are outlined.	38
4.5	Magnitude (a) and relative error (b) of vertical wheel–rail contact force simulated using the ABAQUS 2D model and the previously developed DIFF model. Broadband irregularities with wavelengths in the range 2 cm – 100 cm and amplitudes taken as the limit in ISO3095 [32] is modeled on the rail. Locations of rail seats and nodes of beam elements in the rail FE model are outlined.	39
4.6	Spectrum of the vertical wheel–rail contact force calculated for the ABAQUS 2D model and the DIFF model. Broadband irregularities with wavelengths in the range 2 cm – 100 cm and amplitudes taken as the limit in ISO3095 [32] is modeled on the rail.	39
4.7	Magnitude (a) and relative error (b) of the direct receptance calculated for the 3D ABAQUS model and the DIFF model. The excitation and response are taken at the middle rail seat.	40
4.8	Magnitude (a) and relative error (b) of the static slab track stiffness calculated for the 3D ABAQUS model and the previously developed DIFF model. The boundaries between sections of the concrete panel modeled with solid and beam elements are outlined by vertical lines. .	41

4.9	Magnitude (a) and relative error (b) of vertical wheel–rail contact force simulated using the ABAQUS 3D model and the previously developed DIFF model. Time step 10^{-5} s. The boundaries between sections of the concrete panel modeled with solid and beam elements are outlined by vertical lines.	42
4.10	Magnitude (a) and relative error (b) of vertical wheel–rail contact force simulated using the ABAQUS 3D model and the previously developed DIFF model. Time step 10^{-5} s. Locations of the rail seats and element boundaries are outlined.	42
4.11	Magnitude (a) and relative error (b) of vertical wheel–rail contact force simulated using the ABAQUS 3D model and the previously developed DIFF model. Broadband irregularity with wavelengths in the range 2 cm – 100 cm and amplitudes taken as the limit in ISO3095 [32] is modeled on the rail.	43
4.12	Spectrum of the vertical wheel–rail contact force calculated for the ABAQUS 3D model and the DIFF model. Broadband irregularities with wavelengths in the range 2 cm – 100 cm and amplitudes taken as the limit in ISO3095 [32] is modeled on the rail.	43
4.13	Magnitude (a, c, e) and relative error (b, d, f) of vertical wheel–rail contact force simulated using the ABAQUS 3D model and the previously developed DIFF model. Broadband irregularity with wavelengths in the range 2 cm – 100 cm and amplitudes taken as the limit in ISO3095 [32] is modeled on the rail. Simulations conducted on 3D models with low mesh resolution (a–b), medium mesh resolution (c–d) and high mesh resolution (e–f).	44

List of Tables

3.1	Parameter values of the slab track model developed by Aggestam et al. [27]	23
3.2	Parameter values for the vehicle model used in the dynamic simulations, taken from Iwnicki [31].	34

1

Introduction

In this chapter, the background and motivation will be discussed. Answers to the questions why this work is of importance and how it was carried out are presented.

1.1 Background

Already today, the main railway lines in Sweden are heavily utilized [1]. The Swedish Transport Administration (Trafikverket) has a long-term goal to reduce the fossil fuel reliance within the transport sector, which is expected to be fulfilled partly by an additional increase in transportation by train. With this in mind, new railway lines accommodating high-speed trains connecting the three largest cities in Sweden are planned. This would increase the total capacity of the Swedish railways, both for passenger and freight transportation. Also, because of the decreased travelling time and increased punctuality, trains would become a more attractive way of transportation compared to more fossil fuel dependent alternatives like cars and airplanes.

The track design to be used in a possible future construction of high-speed railway lines in Sweden is currently under investigation. The establishment of a scientific foundation is essential to achieve an optimal design of these railways. High-speed train travel puts heavy demands on the design of both vehicle and track due to their dynamic interaction. Vibrations and large magnitude dynamic forces induced by the wheel–rail contact propagate both upwards, affecting the passenger comfort, and downwards, affecting the track components and the soil underneath the tracks [2]. To mitigate the associated damage in the form of e.g. wear, fatigue and settlements, unconventional track designs are being considered. One alternative is to use so called slab track design, where slabs of prefabricated or cast-on-site concrete is used to support the rails instead of the conventional method of sleepers resting on ballast.

Slab track design has been successfully implemented on several high-speed railway lines located around the world. Advantages with this design are higher lateral track stiffness and no ballast degradation leading to a more stable track geometry with reduced need for track corrective maintenance [3]. Disadvantages are that the initial construction cost is vastly higher due to an increased need of soil improvement and the lack of contractors experienced with the method. Also, rail readjustment is difficult.

In the PhD project CHARMEC TS19 at the department of Mechanics and Maritime Sciences at Chalmers University of Technology in Gothenburg Sweden, the aim is to define design criteria for slab track structures. This is mainly done by studying the vertical dynamic interaction between high-speed vehicles and slab tracks. To this end, a finite element (FE) model representing a slab track design is developed, whose properties are used to calculate transfer functions such as accelerance and receptance, but also dynamic responses, e.g. wheel–rail contact forces, panel bending moment and load distribution on the foundation. Previously in TS19, two types of two-dimensional FE models representing different types of slab track designs have been investigated. In order to perform the dynamic simulations for more realistic conditions, a three-dimensional (3D) model of a slab track structure is developed in the current work.

1.2 Aim

To develop a parameterized 3D model of a slab track structure including rails, rail pads and concrete panels on an elastic foundation using the commercial FE software ABAQUS and Python scripting. Moreover, an interface between ABAQUS and an existing in-house software for simulation of dynamic vehicle–track interaction is to be established.

1.3 Limitations

The software used are limited to Matlab and ABAQUS, scripting is done in Python. Parameter values (material, geometry etc) are taken from CHARMEC TS19. The numerical results will only be compared to previous simulations in CHARMEC TS19. The numerical results of concern are rail receptance, static track stiffness at the rail level and dynamic wheel–rail contact forces.

1.4 Report Layout

The report is divided into six chapters. Chapter 2 presents the theoretical foundation for the dynamic simulations and the finite element modeling. In Chapter 3, the simulation methodology is explained together with the modelling assumptions. Chapter 4 presents the numerical results including a validation of the proposed method. In Chapter 5, the work is summarized and conclusions are drawn. Finally, future work is suggested in Chapter 6.

2

Theory

The following chapter covers the theory that forms a basis for the designed FE model and the conducted dynamic simulations. Also, the design of slab tracks, their geographical spread, and a brief literature review on the chronological evolution of models for the dynamic simulation of vehicle–track interaction are presented.

2.1 Slab Tracks — Design and Historical Review

Traditionally, railway tracks have been composed of rails fastened on wooden or concrete railway ties (sleepers), resting on a bed of ballast. During the 20th century, alternative designs were developed to better suit the specific needs for certain applications.

Such a design is the slab track, which was first introduced in tunnels and on bridges several decades ago. In a slab track design, no ballast is used, allowing the track structure to be easily integrated in a tunnel or a bridge structure. The introduction of high-speed railway lines and the accompanied demands on the tracks provided an incentive to implement slab tracks on embankments and longer distances.

The era of high-speed railways started in Japan in 1964 with the Shinkansen railway, connecting Tokyo and Osaka, a distance of about 500 km [3]. The first lines were built using ties and ballast, but in 1972 slab tracks were first utilized on the Japanese high-speed railway system. The Japanese type slabs were, and still are, discrete 5 m long slabs resting on a concrete roadbed.

Since then, several European countries have introduced high-speed railways. This includes Germany, France, Great Britain, the Netherlands, Spain and Italy. Primarily in Germany and the Netherlands, slab tracks are widely used on the high-speed lines. Recently, the construction of high-speed railway built on slab tracks has expanded in Asia, in countries such as China, Taiwan and South Korea [4].

Advantages of slab tracks frequently mentioned in literature are lower maintenance requirements due to the absence of ballast degradation, thereby increasing track availability and decreasing maintenance costs [3]. The improved track availability is of great importance for the potential construction of new railway lines in Sweden, since it increases capacity and lowers the risk of delays [5]. Also, the track structure height is reduced, allowing tunnel cross sections to be built smaller, cutting construction costs [6]. Furthermore, slab tracks offer higher lateral track stiffness which reduces the risks for sun kinks.

The major disadvantage with slab tracks is the initial construction costs. The track structure itself is usually more expensive, mainly due to inexperience among contractors and manufacturers. However, the largest cost increase comes with the high demands on the track foundation. Settlements on ballastless tracks, contrary to ballasted tracks, cannot be mitigated by simply adding more ballast. Settlements on slab track foundations can therefore be devastating. Consequently, substantial effort must be put on ground improvement on settlement-prone soils.

2.1.1 Common Designs

In current slab track applications, two kinds of designs are dominant. The continuous rail support and the direct rail support systems [3]. The continuous rail support originates from tram applications and provides continuous rail support by embedding rails in an elastomeric layer [7]. Contrary to tracks with discrete support, this implies that a moving wheel does not experience any substantial variation in track stiffness. However, a major disadvantage is that embedded track systems require virtually settlement free soils due to the minimal possibility of rail adjustment. Therefore, continuous rail support systems are not commonly applied for high-speed tracks.

The design type most frequently used on high-speed railways is the direct rail support system, and features discrete connections between rails and concrete slab, either through sleepers or integrated rail seats. The concrete structure can be continuous cast-on-site slabs such as the German Rheda 2000 or pre-fabricated panels of finite length. Prefabrication allows for precise construction in factories followed by fast and controlled installation on site.

One prefabricated system is the Feste Fahrbahn Bögl (FFB) by the German con-

struction company Max-Bögl [8]. The concrete panels are about 6 m long and prefabricated. They are prestressed in the lateral direction and longitudinally coupled on site using force transmitting joints. The support consists typically of a thin layer of grout followed by a hydraulically bound layer (HBL). Depending on the climate zone, the HBL is frequently complemented with a frost protection layer (FPL) and some subgrade foundation underneath.

2.1.2 Typical Components

Typically, a slab-track structure is divided into a super-structure and a sub-structure, see Figure 2.1. This division is important with regard to models of dynamic vehicle-track interaction, as these usually only include the components of the superstructure whereas the substructure is represented by an elastic foundation. In a ballasted track, the sub-structure is usually defined as everything below the sleepers, i.e. the ballast and any subgrade soil underneath it. The rails, rail fasteners, rail pads and railway ties (sleepers or slab tracks) form the super-structure for both ballasted and ballastless tracks to include in e.g a finite element (FE) model of the track structure.

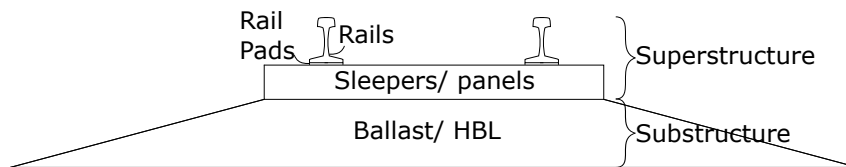


Figure 2.1: Sketch of a track profile divided into a superstructure including rails, rail pads and railway ties and a substructure including the subgrade foundation.

2.2 Historical Modeling of Track Systems

Already in the 19th century, there was an understanding that a fundamental knowledge of railway mechanics is vital to reduce and avoid damages induced to tracks and vehicles. Initially, the main focus was on the train vehicle itself, while the track structure was just considered as a rigid base.

In 1882, Schwedler [9] introduced a model of a ballasted track with the purpose to compute stresses and to identify possible damage mechanisms acting on the different track components including the rails. The model comprised of one rail modeled as an Euler-Bernoulli (E-B) beam laid on sleepers represented by a uniform elastic Winkler-type foundation. It was first around 1930 that the current practice of modeling the rail laid on transverse sleepers represented by a beam on a Winkler

foundation was widely applied [10].

Around the 1960's, researchers tended to shift towards using Rayleigh–Timoshenko (R–T) beams instead of E–B beams in their models. E–B beams perform adequately up to about 500 Hz. At higher frequencies, shear deformations caused by vertical dynamic excitation becomes increasingly important, making the R–T beam, which does take these deformations into account, a better choice.

The application of mathematical modeling to analyze the dynamic vehicle–track interaction became more common in the 1970's. This was partly sparked by the uprise of high-speed railways and the increased magnitude dynamic loads (and associated induced damage) related to an increased vehicle speed. In addition to mechanical damage in the form of e.g. wear, rolling contact fatigue and plastic deformations, the generation of noise and ground-borne vibration represent other issues. The prediction of these phenomena is crucial in order to improve track and vehicle design and to estimate maintenance needs for both tracks and vehicles.

To enable a thorough analysis of the dynamic behavior and the deterioration of tracks and vehicles, a detailed mathematical representation of the vehicle–track system is required. This can be achieved by using the finite element method (FEM). In 1990, Lin and Trethewey [11] incorporated a FE model of elastic beams subjected to a mass–spring–damper system moving at time-dependent speed. They ensued that the interaction problem may be solved by using a numerical time-stepping routine.

In 1995, Nielsen and Igeland [12] solved the dynamic vehicle–track interaction problem numerically using a complex-valued modal superposition of the track. In their work, the track and vehicle were discretized and coupled in large numerical systems of equations. In order to solve the moving load problem for vertical dynamic vehicle–track interaction, an initial value problem was established. The idea of coupling vehicle and track dynamics was adopted by several researchers in the 1990's [2].

2.2.1 Rayleigh–Timoshenko Beam Theory

Beams are the most important structural elements when modeling the static and dynamic behavior of slender structures [13]. Scholl [14] made a comparison using dispersion relations between rail profiles modeled with only beam elements, plate and beam elements, or only plates. This was done in order to establish in which fre-

quency range the respective models accurately represent the rail's dynamic behavior. It was determined that if only vertical vibration is of interest, Rayleigh–Timoshenko (R–T) beams provide adequate results up to about 2.5 kHz. The Euler–Bernoulli (E–B) theory is the most applied approximation beam theory and is valid for slender structures being exerted to vibrations with long wavelengths. However, when the intent is to model thicker, shorter beams, or beams vibrating with a frequency over 500 Hz [10], R–T beam approximation theory is more accurate.

The R–T beam theory differs from the E–B beam theory in two important aspects; it takes shear deformation and rotary inertia into account. This makes the theory more suitable for simulation of the dynamic response at high frequencies, where shearing has a larger influence on the behavior of the structure. In the following paragraphs, a brief walk-through of the basic kinematic differences for R–T beam theory compared to E–B beam theory is presented.

Concerning the kinematics of a R–T beam element in bending, the following assumptions are made [15]:

- All applied loads act transverse to the longitudinal axis.
- All deformations and strains are small.
- Elastic and isotropic material response according to Hooke's law.
- Plane cross sections will remain plane but are not required to remain normal to the longitudinal axis after deformation.

The most important difference to the E–B theory is that plane cross-sections remain plane after deformation, but not required to be normal to the longitudinal axis of the beam. See Figure 2.2 for an illustration of a R–T beam in bending. This implies that shear deformations are being considered, and as a consequence to the assumption that strains are small ($\tan(\psi) \approx \psi$), the fundamental equations for R–T theory are given as [16]

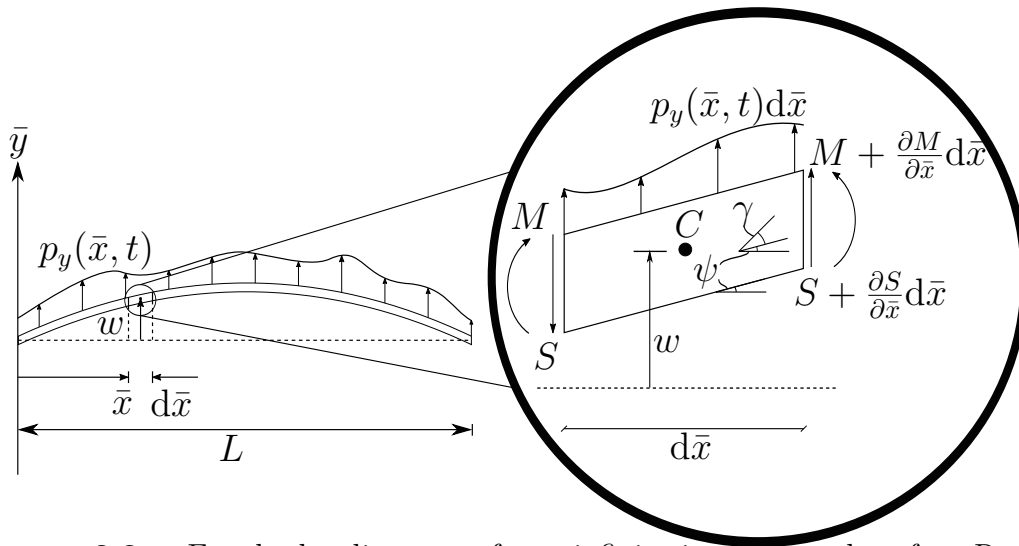


Figure 2.2: Free-body diagram of an infinitesimal part $d\bar{x}$ of a Rayleigh-Timoshenko beam in bending, where \bar{x} marks the longitudinal and \bar{y} marks the transversal direction. The beam is loaded by a transverse force $p_y(\bar{x}, t)$ and has arbitrary boundary conditions. w is the resulting transverse deflection, ψ the resulting bending angle and γ the shear angle. The model also includes the resulting internal shear force S and bending moment M . Inspired by figure 10.17 on page 718 of Benorya and Nagurka [16].

$$-\frac{\partial S}{\partial \bar{x}} + p_y = \rho A \frac{\partial^2 w}{\partial t^2}, \quad (2.1)$$

$$\frac{\partial M}{\partial \bar{x}} - S = \rho I \frac{\partial^2 \psi}{\partial t^2}, \quad (2.2)$$

where \bar{x} is the local longitudinal coordinate, t is time, w is the transverse deflection, p_y is a distributed transverse external load, S and M are the shear force and bending moment resulting from the shear and axial stress, respectively. A is the cross-section area, I is the area moment of inertia, ρ is the density and ψ is the bending angle. Considering the assumptions, the bending moment can be related to the slope of ψ as

$$M = EI \frac{\partial \psi}{\partial \bar{x}}, \quad (2.3)$$

where EI is the bending stiffness. The constitutive relation between the shear angle γ and the shear force is given by

$$S = k'GA\gamma, \quad (2.4)$$

where k' is a scalar that depends on the shape of the cross section [17]. In contrast to E-B theory, the total slope depends on both the bending angle ψ and the shearing angle γ as

$$\gamma = \psi - \frac{\partial w}{\partial \bar{x}}. \quad (2.5)$$

Inserting Eqs. (2.3) to (2.5) in Eqs. (2.1) and (2.2) yield

$$-\frac{\partial}{\partial \bar{x}}[k'GA(\psi - \frac{\partial w}{\partial \bar{x}})] + p_y = \rho A \frac{\partial^2 w}{\partial t^2}, \quad (2.6)$$

$$\frac{\partial}{\partial \bar{x}}(EI \frac{\partial \psi}{\partial \bar{x}}) - k'GA(\psi - \frac{\partial w}{\partial \bar{x}}) = \rho I \frac{\partial^2 \psi}{\partial t^2}. \quad (2.7)$$

The shear force can also be expressed as

$$S = k'(\frac{\partial w}{\partial \bar{x}} - \psi)AG. \quad (2.8)$$

There are several ways of deriving the weak form and the FE form that subsequently will be used, see e.g. Haque [15]. The interpolation polynomials (corresponding to the shape functions of the FEs) used in the current work are given by

$$\begin{aligned} N_{1j} &= \frac{1}{1 + \beta_j} \left(1 - \frac{3\bar{x}_j^2}{l_j^2} + \frac{2\bar{x}_j^3}{l_j^3} \right) + \frac{\beta_j}{1 + \beta_j} \left(1 - \frac{\bar{x}_j}{l_j} \right), \\ N_{2j} &= \frac{1}{1 + \beta_j} \left(-\frac{\bar{x}_j}{l_j} + \frac{2\bar{x}_j^2}{l_j^2} + \frac{3\bar{x}_j^3}{l_j^3} \right) l_j + \frac{\beta_j}{1 + \beta_j} \left(\left[-\frac{x_j}{j} + \frac{x_j^2}{l_j^2} \right] \frac{l_j}{2} \right), \\ N_{3j} &= \frac{1}{1 + \beta_j} \left(\frac{3\bar{x}_j^2}{l_j^2} - \frac{2\bar{x}_j^3}{l_j^3} \right) + \frac{\beta_j}{1 + \beta_j} \frac{\bar{x}_j}{l_j}, \\ N_{4j} &= \frac{1}{1 + \beta_j} \left(\frac{\bar{x}_j^2}{l_j^2} - \frac{\bar{x}_j^3}{l_j^3} \right) l_j + \frac{\beta_j}{1 + \beta_j} \left(\left[\frac{x_j}{l_j} - \frac{x_j^2}{l_j^2} \right] \frac{l_j}{2} \right), \end{aligned} \quad (2.9)$$

where $\beta_j = 12EI/(k'GA l_j^2)$, l_j is the length of the beam element in the FE model of the rail and $\bar{x}_j \in [0, l_j]$ is the local coordinate of the beam element. A derivation of the interpolation polynomials was done by Sällström [18].

2.2.2 Winkler Foundation

The Winkler foundation is commonly applied in FE simulations to model an elastic distributed support. According to the Winkler-model, the sub grade is idealized as a system of mutually independent, continuously distributed, linear springs [19]. The linear relationship between the force on the foundation p_f and the deflection of the beam w is given by

$$p_f(\bar{x}, t) = k_w b(\bar{x}, t) w(\bar{x}, t), \quad (2.10)$$

where b is the width of the beam and k_w is the bed modulus. Figure 2.3 illustrates how the Winkler foundation can be incorporated in the fundamental formulation for the R–T beam.

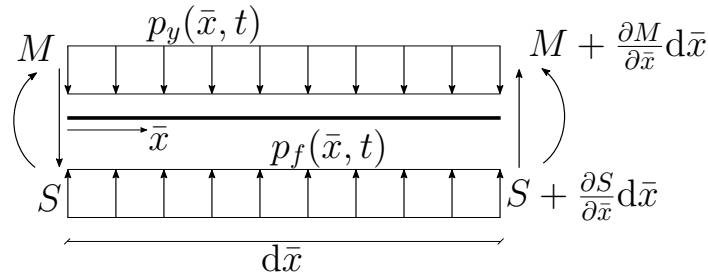


Figure 2.3: An infinitesimal part of a R–T beam element subjected to a transverse uniformly distributed load p_y , resting on an elastic foundation with an uniformly distributed reaction load p_f .

The foundation force p_f can now be added to Eq. (2.6) as

$$-\frac{\partial}{\partial \bar{x}} \left[k'GA \left(\psi - \frac{\partial w}{\partial \bar{x}} \right) \right] + p_y - p_f = \rho A \frac{\partial^2 w}{\partial t^2}. \quad (2.11)$$

2.3 Simulation of Dynamic Vehicle–Track Interaction

The dominant frequency components in the vibration generated during train operation vary between the different parts of the vehicle–track system. The bogie’s primary suspension is typically designed such that the fundamental modes of vibration occur below 10 Hz [10], see Figure 2.4 for an illustration of a vehicle. This will isolate passengers from vibration and also reduce the effective unsprung mass which is beneficial for decreasing the dynamic loads at the wheel–rail contact interface. With respect to running stability, steering and passenger comfort, it is sufficient to account for frequencies up to only a few Hertz. At these low frequencies, the track acts like a stiff spring. At frequencies over 20 Hz the track’s inertia becomes more important and thus a threshold between vehicle stability issues and the estimation and prediction of rail damage can be drawn at about 20 Hz.

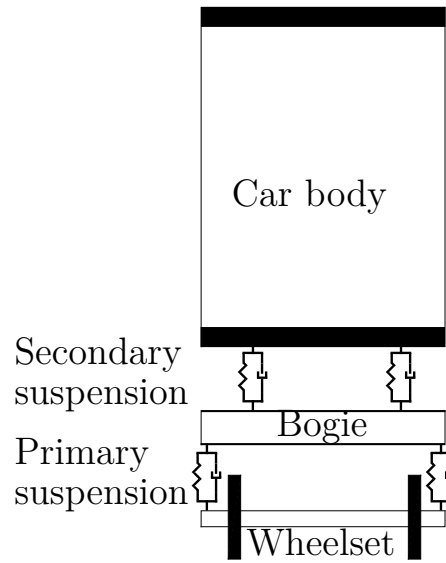


Figure 2.4: Sketch of a vehicle model including the car body, bogie and wheelset. The wheelset and the bogie frame are attached to the car body via the primary and secondary suspensions.

In order to investigate effects of imperfections as e.g. wheel flats and rail corrugation, it is required to account for dynamic vehicle–track interaction at higher frequencies than 20 Hz. For example, numerous models have been proposed in literature to study wheel flats generated due to locking brakes [20]. Another issue of concern is rolling contact fatigue (e.g. pitting, squats and shelling), which are caused by the large number of load cycles corresponding to wheelset passages (for rail material) or wheel revolutions (for wheel material) [21]. On all types of railways, short wavelength (20-100mm) irregularities that develop on the rail running surface (corrugation) is a concern [22]. The generation of corrugation is a combination of dynamic loading and an acting damage mechanism.

In the frequency range exceeding 1500 Hz, issues concerning noise and ground vibrations are a concern. The analyzed frequency range may extend up to the human limit of hearing, at about 20 kHz. However, while these factors play a major role in acoustic railway engineering, it is in railway mechanics considered to be sufficient to include the frequency range up to 1500 Hz.

2.3.1 Normal Wheel–Rail Contact

The contact between a rigid wheel and a rigid rail without imperfections is a line, which indicates that the pressure on the surfaces will be infinite. In reality, a small contact area is formed due to the elastic properties of the connected surfaces, thus reducing the pressure exerted on them [23]. The linear-elastic contact model developed by Hertz is briefly presented in this section.

In classic Hertzian theory, contact is considered non-adhesive, i.e. no tension force is allowed to occur within the contact area. In this theory, the following assumptions are made in [24]:

- The contact area is elliptical.
- The strains are small and do not surpass the yield limit.
- Each body can be considered as an elastic half space, i.e., the contact areas are considerably smaller than the relative radii of the bodies.
- The surfaces are continuous and non-conforming.
- There is no friction between surfaces.
- The surfaces are smooth, i.e surface roughness is ignored.
- Deformation is purely elastic.
- The contacting bodies' materials are homogeneous and isotropic.
- The bodies are geometrically (consequence of the half-space assumption) and elastically identical.

In Johnson [25], the normal contact stiffness $k_{\text{CH, theory}}$ for an ellipsoidal contact between two geometries is defined as

$$k_{\text{CH, theory}} = \frac{2E^*c}{F_1F_2} \quad (2.12)$$

where F_1 and F_2 are correction factors that depend on the shape of the ellipse ($F_1=F_2=1$ if the contact is a circle), while E^* is the equivalent Young's modulus when combining the two materials. E^* is defined as follows, where subscripts 1 and 2 denotes the wheel and rail, respectively, and ν the Poisson's ratio:

$$\frac{1}{E^*} = \frac{1 - \nu_1^2}{E_1} + \frac{1 - \nu_2^2}{E_2}.$$

Furthermore, c is the equivalent radius of contact defined as

$$c = \left(\frac{3NR_m^*}{4E^*} \right)^{\frac{1}{3}} F_1 \quad (2.13)$$

where N is the applied normal load and R_m^* is defined as the equivalent mean radius of the curvature of the contact geometries according to

$$R_m^* = \sqrt{R_x^* R_z^*} \quad \text{where} \quad (2.14)$$

$$\frac{1}{R_x^*} = \frac{1}{R_{x1}} + \frac{1}{R_{x2}} \quad \text{and} \quad (2.15)$$

$$\frac{1}{R_z^*} = \frac{1}{R_{z1}} + \frac{1}{R_{z2}} \quad (2.16)$$

where R^x and R^z are the contact radii in the two contact orientations x and z of the wheel and rail, according to Figure 2.5.

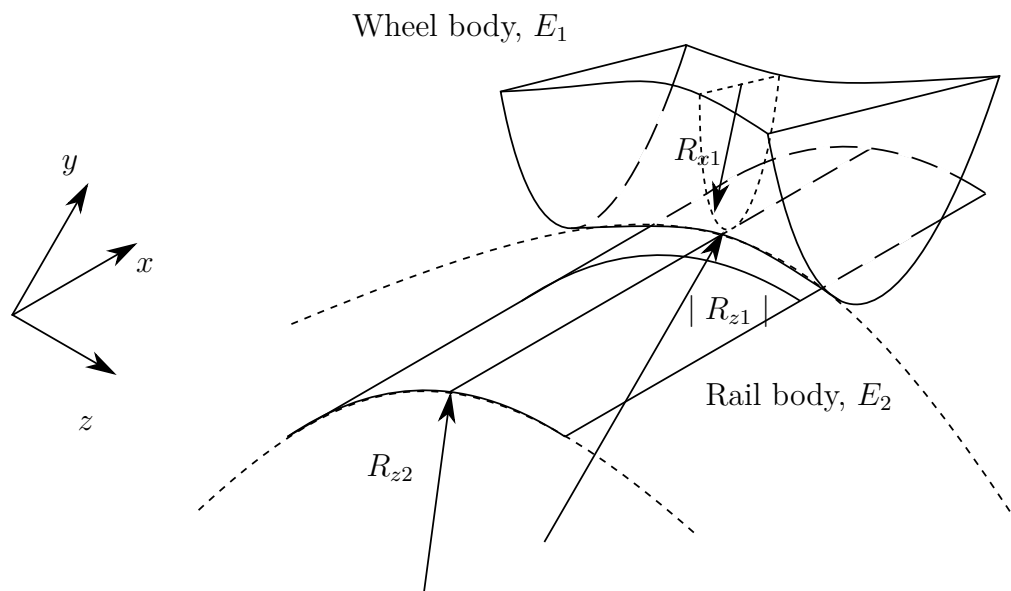


Figure 2.5: Sketch of a contact between a wheel and a rail. The wheel has radii R_{x1} in the (x, y) -plane and R_{z1} (sometimes negative) in the (z, y) -plane while the rail has radii R_{z2} in the (z, y) -plane and $R_{x2} = \infty$ in the (x, y) -plane. The coordinates x, y, z are outlined. The illustration is inspired by a figure in Andersson et al. [24].

As no surface is completely smooth, the value of $k_{\text{CH, theory}}$ will not hold in reality. Greenwood and Tripp [26] analyzed the contact stiffness considering a rough interface and concluded that up to a certain load, the actual Hertzian contact stiffness is approximately one-third of $k_{\text{CH, theory}}$. However, since this approximation is load dependant, the actual stiffness varies between the theoretical and the value given by Greenwood and Tripp [26].

$$\frac{k_{\text{CH, theory}}}{3} < k_{\text{CH, actual}} < k_{\text{CH, theory}} \quad (2.17)$$

2.3.2 Time-Integration of the Coupled Vehicle–Track System

The moving load problem of a vehicle traversing a track modeled using FEs results in a large system of coupled differential equations. In order to solve the dynamic vehicle–track interaction using less computational capacity, the number of degrees of freedom (DOFs) of the track is reduced through a complex-valued modal superposition. The modal superposition must be complex-valued due to the non-proportional distribution of damping in the FE model. Furthermore, to attain a discrete spectrum of eigenvalues, a finite length for the whole model must be used.

For a structural system discretized to an FE model, the governing differential equations of motion can be written as

$$\mathbf{M}\ddot{\mathbf{x}}(t) + \mathbf{C}\dot{\mathbf{x}}(t) + \mathbf{K}\mathbf{x}(t) = \mathbf{F}(t), \quad (2.18)$$

where \mathbf{K} , \mathbf{C} and \mathbf{M} are the global stiffness, damping and mass matrices respectively, $\mathbf{F}(t)$ is the global load vector and $\mathbf{x}(t)$ is a vector containing the structural displacement. If $\mathbf{x}^t(x)$ (superscript t denotes track) is a vector containing the DOFs and $\mathbf{F}^t(t)$ contains the external loads, Eq. (2.18) for the track can be rewritten in state-space form as

$$\mathbf{A}^t \mathbf{y}^t(t) + \mathbf{B}^t \mathbf{y}^t(t) = \begin{Bmatrix} \mathbf{F}^t(t) \\ 0 \end{Bmatrix}, \quad (2.19)$$

where

$$\mathbf{y}^t(t) = \begin{Bmatrix} \mathbf{x}^t \\ \dot{\mathbf{x}}^t(t) \end{Bmatrix}, \mathbf{A}^t = \begin{bmatrix} \mathbf{C}^t & \mathbf{M}^t \\ \mathbf{M}^t & \mathbf{0} \end{bmatrix}, \mathbf{B}^t = \begin{bmatrix} \mathbf{K}^t & \mathbf{0} \\ \mathbf{0} & -\mathbf{M}^t \end{bmatrix}. \quad (2.20)$$

Considering that \mathbf{A}^t and \mathbf{B}^t are symmetric, the complete modal solution to Eq. (2.19) can be written as follows (where superscript -1 denotes the matrix inverse and underline indicates complex quantities):

$$\begin{bmatrix} \mathbf{K}^{t-1} \mathbf{C}^t & \mathbf{K}^{t-1} \mathbf{M}^t \\ -\mathbf{I} & \mathbf{0} \end{bmatrix} \begin{Bmatrix} \underline{\boldsymbol{\rho}}^{(n)} \\ i\underline{\omega}_n \underline{\boldsymbol{\rho}}^{(n)} \end{Bmatrix} = -\frac{1}{i\underline{\omega}_n} \begin{Bmatrix} \underline{\boldsymbol{\rho}}^{(n)} \\ i\underline{\omega}_n \underline{\boldsymbol{\rho}}^{(n)} \end{Bmatrix}, \quad (2.21)$$

where $\underline{\omega}_n$ are angular eigenfrequencies, $\underline{\boldsymbol{\rho}}^{(n)}$ are eigenvectors and \mathbf{I} is the unit matrix. When the eigenvalue problem in Eq. (2.21) is solved, the modal matrix $\underline{\mathbf{P}}$, can be assembled. This matrix works as a mapping between the spatial and modal domains

as

$$\mathbf{y}^t(t) = \underline{\mathbf{P}}\underline{\mathbf{q}}^t(t), \quad \underline{\mathbf{Q}}^t(t) = \underline{\mathbf{P}}^T = \begin{Bmatrix} \mathbf{F}^t(t) \\ 0 \end{Bmatrix}, \quad (2.22)$$

where $\underline{\mathbf{Q}}^t$ is the modal load vector. Due to orthogonality of the modal matrix, the equations of motion can be written as

$$\text{diag}(\underline{a}_n)\underline{\dot{\mathbf{q}}}^t(t) + \text{diag}(\underline{b}_n)\underline{\mathbf{q}}^t(t) = \underline{\mathbf{Q}}^t(t), \quad (2.23)$$

where

$$\text{diag}(\underline{a}_n) = \underline{\mathbf{P}}^T \mathbf{A}^t \underline{\mathbf{P}}, \quad (2.24)$$

and

$$\text{diag}(\underline{b}_n) = \underline{\mathbf{P}}^T \mathbf{B}^t \underline{\mathbf{P}}. \quad (2.25)$$

Here, \underline{a}_n and \underline{b}_n are so-called modal Foss dampings and modal Foss stiffnesses. When $\underline{\mathbf{Q}}^t(t)$ and $\underline{\mathbf{q}}^t(t)$ have been computed, they will subsequently be used to determine physical displacements, velocities and accelerations.

The vehicle model consists of one bogie with two wheelsets as seen in Figure 2.6. The bogie and wheelsets are considered rigid and the vehicle can be expanded to include a full car with the car body and two bogies. However, because the secondary suspension acts as a dynamic filter isolating the car body from the bogie in the frequency range where the dynamics of the track is significant, only one bogie is used. The DOFs of the vehicle are divided into two vectors: $\mathbf{x}_a^v = \{x_{a1} x_{a2}\}^T$ which contains two massless DOFs that are interfacing with the track and $\mathbf{x}_b^v = \{x_{b1} x_{b2} x_{b3} x_{b4}\}^T$ which contains the DOFs representing the wheelsets and the bogie which will not be in contact with the track (superscript v denotes vehicle and T denotes the matrix transpose). The equations of motion of the vehicle can be written as

$$\begin{bmatrix} \mathbf{0} & \mathbf{0} \\ \mathbf{0} & \mathbf{M}_{bb}^v \end{bmatrix} \begin{Bmatrix} \ddot{\mathbf{x}}_a^v(t) \\ \ddot{\mathbf{x}}_b^v(t) \end{Bmatrix} + \begin{bmatrix} \mathbf{0} & \mathbf{0} \\ \mathbf{0} & \mathbf{C}_b^v \end{bmatrix} \begin{Bmatrix} \dot{\mathbf{x}}_a^v(t) \\ \dot{\mathbf{x}}_b^v(t) \end{Bmatrix} + \begin{bmatrix} \mathbf{K}_{aa}^v & \mathbf{K}_{ab}^v \\ \mathbf{K}_{ba}^v & \mathbf{K}_{bb}^v \end{bmatrix} \begin{Bmatrix} \mathbf{x}_a^v \\ \mathbf{x}_b^v \end{Bmatrix} + \begin{Bmatrix} \mathbf{F}_a(t) \\ \mathbf{0} \end{Bmatrix} = \begin{Bmatrix} \mathbf{0} \\ \mathbf{F}_b^{\text{ext}} \end{Bmatrix}. \quad (2.26)$$

Here, $\mathbf{F}_a(t)$ are contact forces between the wheels and rail while $\mathbf{F}_b^{\text{ext}}$ contains the gravity loads. The Hertzian contact stiffness k_{Hi} ($i = 1, 2$) is embedded in \mathbf{K}^v and is given by:

$$k_{Hi} = \begin{cases} C_H(x_{bi} - x_{ai}) & \text{for } x_{bi} - x_{ai} > 0 \\ 0 & \text{else} \end{cases}, \quad (2.27)$$

where C_H is defined according to Section 2.3.1

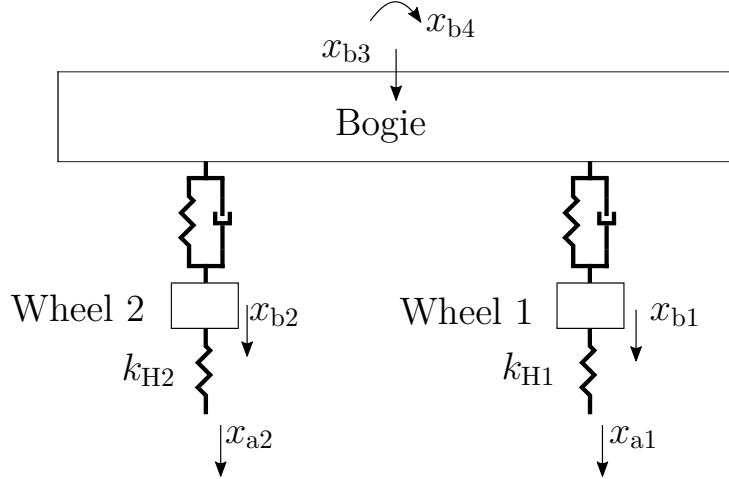


Figure 2.6: Sketch of the vehicle model. The model consists of one bogie, and both wheels and bogie frame are rigid bodies. x_{a1} and x_{a2} are mass-less DOFs in contact with the rail through springs with stiffness k_{H1} and k_{H2} respectively. DOFs x_{b1} , x_{b2} are the vertical displacements of wheelset 1 and 2, respectively, and DOFs x_{b3} and x_{b4} are the vertical displacement and pitch rotation of the bogie frame, respectively.

To couple the vehicle and track models, constraints on contact velocities and accelerations between vehicle and track are formulated. Due to the FE format of the track model, the continuously moving contact forces are converted into stationary time-dependent forces located at the two closest nodes to the actual position of the moving force. The deflection shape between two adjacent nodes is computed by using the interpolation polynomials introduced in Equation (2.9).

The selected constraints on the transverse velocities and accelerations at the connecting DOFs yield [12]

$$\dot{\mathbf{x}}_a(t) = \underline{\mathbf{T}}(t)\dot{\underline{\mathbf{q}}}(t) + \underline{\mathbf{U}}(t)\underline{\mathbf{q}}(t) + \dot{\mathbf{x}}^{\text{irr}}, \quad (2.28)$$

where

$$\underline{\mathbf{T}}(t) = \underline{\mathbf{N}}\underline{\mathbf{P}}^{\text{int}}, \quad (2.29)$$

$$\underline{\mathbf{U}}(t) = \left(\frac{d\underline{\mathbf{N}}}{d\bar{x}} \right) v \underline{\mathbf{P}}^{\text{int}}, \quad (2.30)$$

and

$$\ddot{\mathbf{x}}_a(t) = \underline{\mathbf{R}}(t)\dot{\mathbf{q}}^t(t) + \underline{\mathbf{S}}(t)\mathbf{q}^t(t) + \ddot{\mathbf{x}}^{\text{irr}}, \quad (2.31)$$

$$\underline{\mathbf{R}}(t) = 2 \left(\frac{d\mathbf{N}}{d\bar{x}} \right) v \underline{\mathbf{P}}^{\text{int}} + \mathbf{N} \underline{\mathbf{P}}^{\text{int}} \text{diag}(i\omega_n), \quad (2.32)$$

$$\underline{\mathbf{S}}(t) = \left(\frac{d^2\mathbf{N}}{d\bar{x}^2} \right) v^2 \underline{\mathbf{P}}^{\text{int}} + \frac{d\mathbf{N}}{d\bar{x}} \dot{v}(t) \underline{\mathbf{P}}^{\text{int}}(t). \quad (2.33)$$

In the equations above, $\underline{\mathbf{P}}^{\text{int}}$ is the partition of the modal matrix in Equation (2.22) containing the interfacial vehicle DOFs, $\underline{\mathbf{R}}(t)$ contains the Coriolis acceleration and the vertical acceleration of the railhead and the centripetal and longitudinal acceleration is included in $\underline{\mathbf{S}}(t)$.

Prescribed contact irregularities such as wheel flats and rail corrugation may be included in the model by using irregularity functions assembled in \mathbf{x}^{irr} . The contact forces are distributed onto the rail nodes by using the interpolation polynomials, and the modal load vector from Section 2.3.2 can now be obtained as:

$$\underline{\mathbf{Q}}^t = \underline{\mathbf{P}}^{\text{intT}} \mathbf{N}^T \mathbf{F}_a(t). \quad (2.34)$$

To solve the interaction problem, the equations of motion, cf. Eqs. (2.19) and (2.23) and the algebraic constraint equations, cf. Eqs. (2.28) and (2.31) may be assembled in matrix format using the extended state-space vector $\underline{\mathbf{z}}$:

$$\underline{\mathbf{z}} = \left\{ \underline{\mathbf{q}}^{tT} \mathbf{x}_a^{vT} \mathbf{x}_b^{vT} \dot{\mathbf{x}}_a^{vT} \dot{\mathbf{x}}_b^{vT} \hat{\mathbf{F}}_a^T \right\}^T, \quad (2.35)$$

which includes not only displacements and velocities but also impulses $\hat{\mathbf{F}}_a = \int \mathbf{F}_a(t) dt$ of the contact forces. The total coupled and time-dependant system is now written as:

$$\underline{\mathbf{A}}(\underline{\mathbf{z}}, t) \dot{\underline{\mathbf{z}}} + \underline{\mathbf{B}}(\underline{\mathbf{z}}, t) \underline{\mathbf{z}} = \underline{\mathbf{F}}(\underline{\mathbf{z}}, t), \quad (2.36)$$

where

$$\underline{\mathbf{A}}(\underline{\mathbf{z}}, t) = \begin{bmatrix} \underline{\mathbf{A}}_{11} & \underline{\mathbf{A}}_{12} \\ \underline{\mathbf{A}}_{21} & \underline{\mathbf{A}}_{22} \end{bmatrix} = \left[\begin{array}{c|cccc} \text{diag}(a_n) & \mathbf{0} & \mathbf{0} & \mathbf{0} & \mathbf{0} & -\underline{\mathbf{P}}^{\text{intT}} \mathbf{N}^T \\ \hline \mathbf{0} & \mathbf{0} & \mathbf{0} & \mathbf{0} & \mathbf{0} & \mathbf{I} \\ \mathbf{0} & \mathbf{0} & \mathbf{C}_{\text{bb}}^v & \mathbf{0} & \mathbf{M}_{\text{bb}}^v & \mathbf{0} \\ \mathbf{0} & \mathbf{0} & \mathbf{I} & \mathbf{0} & \mathbf{0} & \mathbf{0} \\ \underline{\mathbf{R}} & \mathbf{0} & \mathbf{0} & -\mathbf{I} & \mathbf{0} & \mathbf{0} \\ \mathbf{N} \underline{\mathbf{P}}^{\text{int}} & -\mathbf{I} & \mathbf{0} & \mathbf{0} & \mathbf{0} & \mathbf{0} \end{array} \right], \quad (2.37)$$

$$\underline{\mathbf{B}}(z, t) = \begin{bmatrix} \underline{\mathbf{B}}_{11} & \underline{\mathbf{B}}_{12} \\ \underline{\mathbf{B}}_{21} & \underline{\mathbf{B}}_{22} \end{bmatrix} = \left[\begin{array}{c|ccccc} \text{diag}(b_n) & \mathbf{0} & \mathbf{0} & \mathbf{0} & \mathbf{0} & \mathbf{0} \\ \hline \mathbf{0} & \mathbf{K}_{aa}^v & \mathbf{K}_{ab}^v & \mathbf{0} & \mathbf{0} & \mathbf{I} \\ \mathbf{0} & \mathbf{K}_{ba}^v & \mathbf{K}_{bb}^v & \mathbf{0} & \mathbf{0} & \mathbf{0} \\ \mathbf{0} & \mathbf{0} & \mathbf{0} & \mathbf{0} & -\mathbf{I} & \mathbf{0} \\ \underline{\mathbf{S}} & \mathbf{0} & \mathbf{0} & \mathbf{0} & \mathbf{0} & \mathbf{0} \\ \frac{dN}{dt}v(t)\underline{\mathbf{P}}^{\text{int}} & \mathbf{0} & \mathbf{0} & \mathbf{0} & \mathbf{0} & \mathbf{0} \end{array} \right], \quad (2.38)$$

$$\underline{\mathbf{F}}(z, t) = \begin{bmatrix} \underline{\mathbf{F}}_1^T \\ \underline{\mathbf{F}}_2^T \end{bmatrix} = \left[\mathbf{0}^T \mid \mathbf{0}^T \quad \mathbf{F}_b^{\text{extT}} \quad \mathbf{0}^T - \ddot{\mathbf{x}}^{\text{irrT}} - \dot{\mathbf{x}}^{\text{irrT}} \right]^T. \quad (2.39)$$

The initial value problem to solve the transient vibration problem is now formulated as:

$$\dot{\mathbf{z}} = \underline{\mathbf{A}}^{-1}(\underline{\mathbf{F}} - \underline{\mathbf{B}}\mathbf{z}), \quad \mathbf{z}|_{t=0} = \mathbf{z}_0, \quad (2.40)$$

where \mathbf{z}_0 is the initial state. Considering that the modal solution results in complex-conjugate sets of modal parameters, the real and imaginary parts of Eq. (2.23) and Eqs. (2.28) to (2.33) can be separated which makes the initial value problem in Eq. (2.40) real-valued. Solutions are obtained using an ordinary differential equation solver with variable step size. To save computation time, the matrix $\underline{\mathbf{A}}$ is partially inverted when Eq. (2.40) is established instead of inverting the full matrix at every instant of time.

3

Method

In the following chapter, the proposed numerical procedure is presented. The different steps of the adopted methodology are summarized in the flow chart in Figure 3.1.

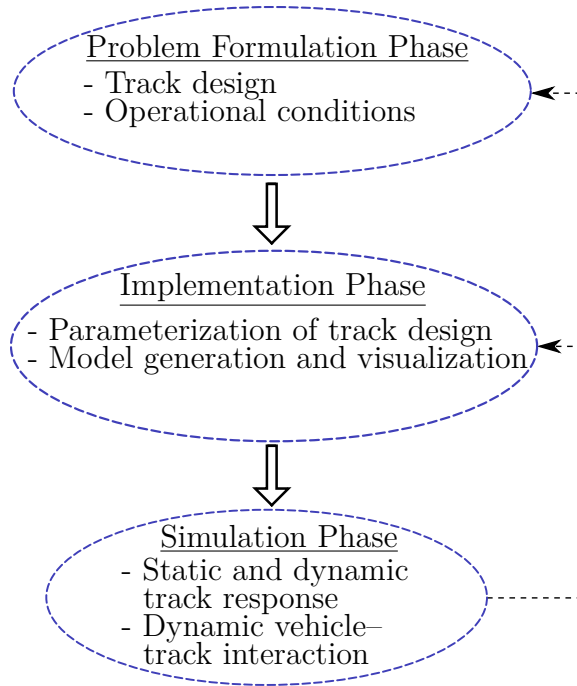


Figure 3.1: Sketch of the proposed simulation procedure. First, the problem is set by determining the track design and operational conditions. In the implementation phase, the track model is parameterized in a Python script, and then generated in ABAQUS. The model is subsequently exported to Matlab for dynamic and static track simulations. Ultimately, the model can be altered based on simulation results.

The problem is formulated by determining the track design and operational conditions. For determining the track design, the German-manufactured Max-Bögl Feste Fahrbahn (FFB) slab track system briefly described in Section 2.1.1 and in reference [8] is the starting point. More on how the design is adopted is covered in the next section where a description of the existing model developed in the CHARMEC

project TS19 is presented.

3.1 Previously Developed DIFF model

In CHARMEC TS19, the aim is to find design criteria for future slab track designs. The chosen method is to do so by analyzing the vertical dynamic vehicle–track interaction. To solve the problem at hand, the track structure is numerically approximated as a finite element (FE) model. A slab track corresponding to the FFB slab track system, with a track profile according to Fig. 3.2, is adopted by Aggestam et al. [27].

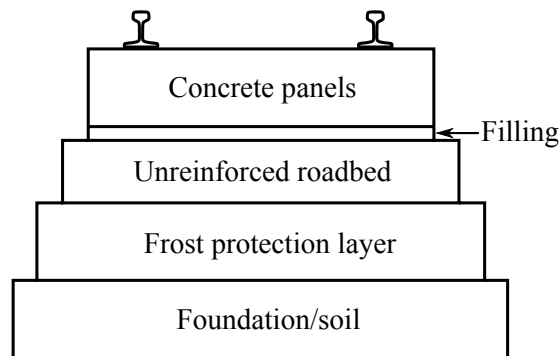


Figure 3.2: Profile sketch of a slab track of German design with hydraulically bound layer (unreinforced roadbed in this sketch). Figure from Aggestam et al. [27].

This two-dimensional (2D) FE model, hereon referred to as the DIFF model, is throughout the current work used for benchmarking the developed models. Moreover, the DIFF model is used for simulation of dynamic vehicle–track interaction in the proposed numerical procedure. In this model, Rayleigh–Timoshenko beam elements are used to represent both the rail and the concrete panels. The discrete rail seats are modeled by parallel springs and viscous dampers. The foundation is modeled by a Winkler foundation, with potentially variable stiffness and damping depending on the longitudinal coordinate x . A sketch of the track model is seen in Figure 3.3.

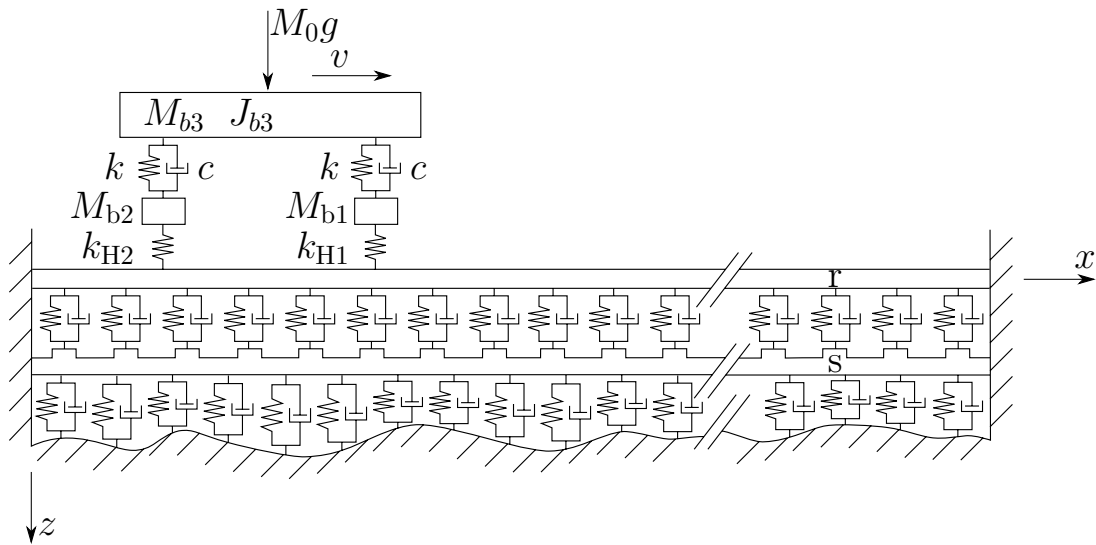


Figure 3.3: Sketch of the DIFF slab track model. The model consists of two layers of beams representing the rail (r) and the concrete panel (s). The concrete panel is supported by a Winkler foundation, where the prescribed (possibly random) variation in stiffness is indicated by the irregular ground surface. Figure from Aggestam et al. [27].

The parameter values of the track are selected to be as realistic as possible. However, no experimental calibration/validation has yet been performed. The parameter values of the track are shown in Table 3.1. The full track structure consists of 120

Table 3.1: Parameter values of the slab track model developed by Aggestam et al. [27]

Parameter	Value	Legend
EI_s	30 MNm ²	Bending stiffness, concrete slab
EI_r	6.4 MNm ²	Bending stiffness, rail
kGA_s	2.1 GN	Shear stiffness, concrete slab
kGA_r	250 MN	Shear stiffness, rail
k_r	0.4 [-]	Shear constant, rail
m_s	580 kg/m	Mass per meter, concrete slab
m_r	60 kg/m	Mass per meter, rail
b_s	1.2 m	Width, concrete slab
h_s	0.2 m	Height, concrete slab
k_{r/s_1}	40 MN/m	Spring stiffness between the rail and the concrete slab
c_{r/s_1}	10 kNs/m	Damping coefficient between the rail and the concrete slab
k_f	100MN/m ³	Spring stiffness, elastic foundation
c_f	82kN/m ³	Damping coefficient, elastic foundation

rail seats each spanning 0.65 m, which renders a total track length of 78 m. The

length has been determined to be sufficiently long in order to attenuate boundary effects (reflections) that might affect the simulation results. By modeling the track using FEs, the quality of the calculated results will depend on the discretization (element size). The conversion of the moving contact forces into spatially stationary time-dependent nodal forces (mentioned in Section 2.3) implies that the true local deflection under the contact force is somewhat underestimated [12]. To limit this effect, a common procedure is to increase the mesh resolution. The boundaries at both ends of the rail and the panel are fixed, i.e both translational and rotational DOFs are constrained.

3.2 Implementation Phase

A requirement of the methodology developed in the current work has been that it should enable to generate a parameterized three dimensional slab track model. This is to allow for parametric studies as model properties such as geometries and materials can be easily altered. For this purpose, Python scripts are used to generate FE models in ABAQUS.

ABAQUS is a commercial FE analysis software suite developed by Dassault Systèmes Simulia Corp [28]. It can be used to conduct linear and non-linear analysis of models with complex geometries. What makes ABAQUS suitable for the current project is that it has an application programming interface (API), which is an extension of the object oriented programming language Python.

The ABAQUS scripting procedure is summarized in Figure 3.4. The user can write a Python script with commands and parameters that is interpreted in the API, or use the ABAQUS graphical user interface (GUI) to generate the Python script which is interpreted in the API. All the actions done by the Python interpreter is recorded in a replay file. This offers a good way of learning the commands necessary for scripting since all actions in the GUI are recorded as Python commands. Furthermore, Python commands can be directly typed in the ABAQUS GUI, enabling visual confirmation of the actions triggered by the command.

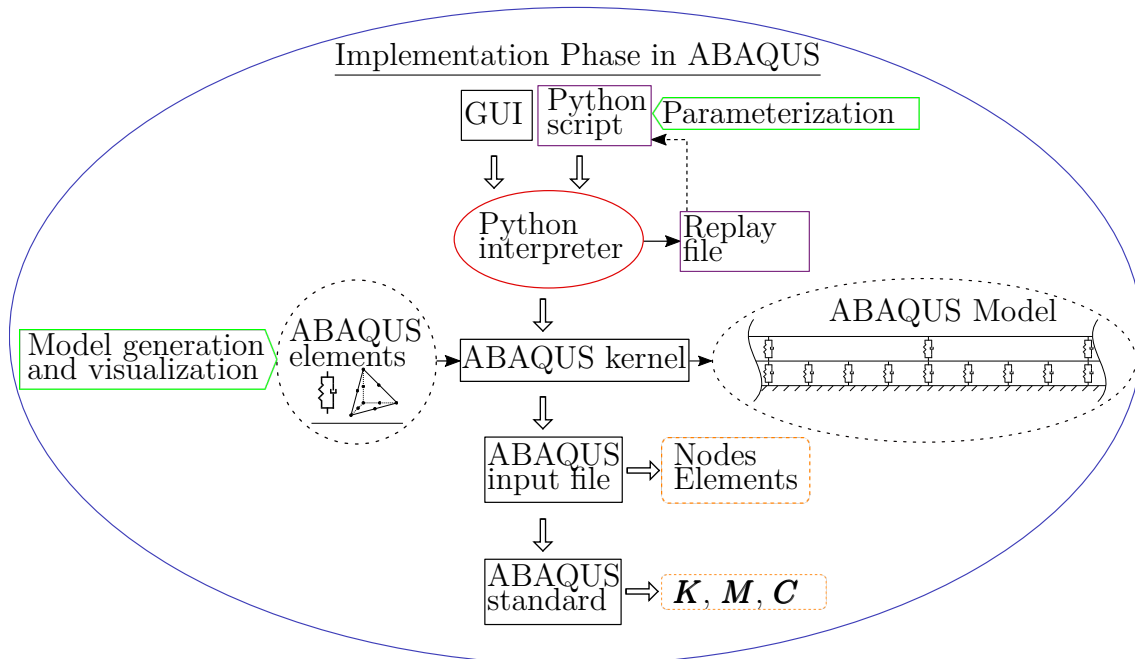


Figure 3.4: Diagram sketch of the implementation phase in ABAQUS.

The information is then processed in the ABAQUS kernel, where the interpreted script is used to generate the ABAQUS model out of ABAQUS elements and commands. The kernel generates an ABAQUS input (.inp) file which contains all the information about element types, node coordinates, mesh topology and material properties of the model to be analyzed. The input file can be read in Matlab, thereby exporting node and element information which is used to sort the mechanical system matrices (K , M and C) in Matlab.

The input file can also be run in ABAQUS standard analysis to calculate the structural dynamic and static displacement and stress response. In this application, system matrices are generated and exported to Matlab for use in static and dynamic simulations.

3.2.1 Two-dimensional Slab Track Model

In order to verify the implementation in ABAQUS, the initial step of the current project was to duplicate the 2D DIFF model in Aggestam et al. [27]. To this end, spring-dashpot and beam elements with properties governed by user set constants were used in ABAQUS. The beam elements are R-T beams with three DOFs per node (see Fig. 3.5) denoted B21 in ABAQUS.

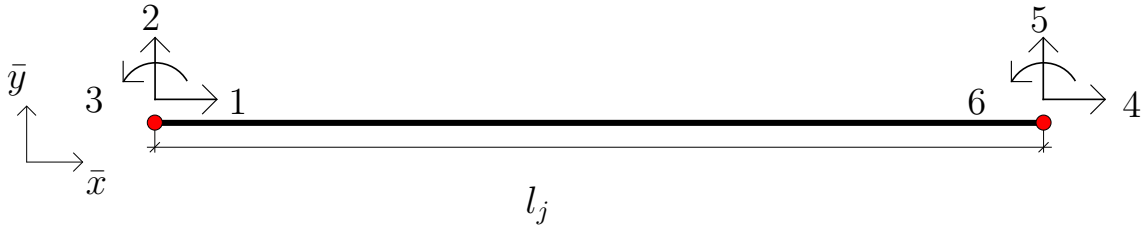


Figure 3.5: Sketch of a R-T 2D beam element with two nodes, each consisting of two translational and one rotational DOF. \bar{x} and \bar{y} denote the local spatial coordinates and l_j denotes the element length.

Parameter values are taken from Table 3.1 and implemented in ABAQUS using generalized beam sections which are assigned to the beam elements for the rail and concrete panel, respectively. Each section has an arbitrary beam profile, which in turn is assigned values for cross-sectional area, area of inertia and torsional rigidity. Furthermore, the shear coefficient is accounted for by specifying the transverse shear and setting the shear factor. In Equation (2.8), the product $k'A$ can be manipulated through the parameter SCF which is defined as [29]

$$SCF = \frac{k'GA}{G}, \quad (3.1)$$

and is implemented in the definition of transverse shear for beams in ABAQUS.

The second element used is the connector element CONN2D2 which connects nodes of different parts in ABAQUS. The connector elements can be assigned different properties to model springs and/or dampers. It is necessary to set the direction in which the element acts. In this implementation, it is defined with respect to the global cartesian coordinates. In the 2D model, one CONN2D2 element represents one rail pad by connecting one rail node to a corresponding panel node at each rail seat, see Figure 3.6.

Furthermore, the Winkler foundation is approximated as CONN2D2 elements connecting each panel node to the ground (mass-less nodes constrained in all DOFs) as seen in Figure 3.7. In the current implementation, all ground connectors have the same properties.

Consequent to the DIFF model, the current model consists of 120 rail seat distances, spanning a total length of 78 m. Both ends of the rail and concrete panel are fixed, which is seen Figure 3.8.

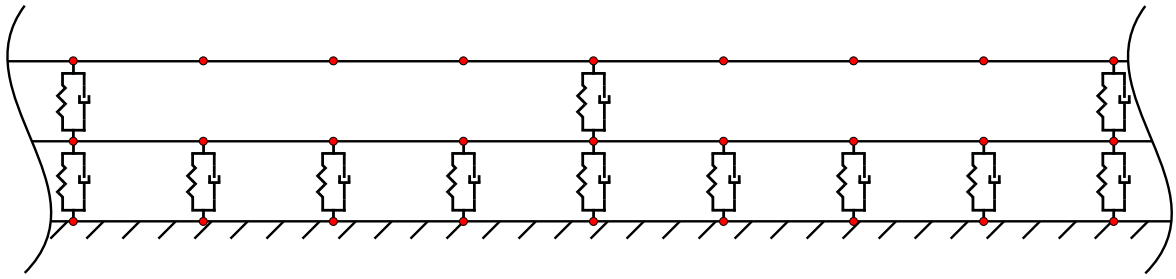


Figure 3.6: Magnified sketch of the 2D ABAQUS slab track model covering two rail seat distances. The upper beam layer represents the rail and the lower represents a continuous concrete slab. The rail and the slab are connected by a spring–dashpot pair at each rail seat while the slab and the ground are connected by a spring–dashpot pair at each element node as a substitute for a Winkler foundation.

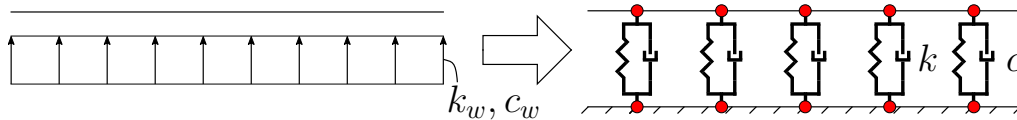


Figure 3.7: Sketch of the foundation adapted in ABAQUS. The Winkler bed is approximated as spring/dashpot pairs coupling each node of the concrete panel to the ground represented by mass-less nodes constrained in all DOFs.

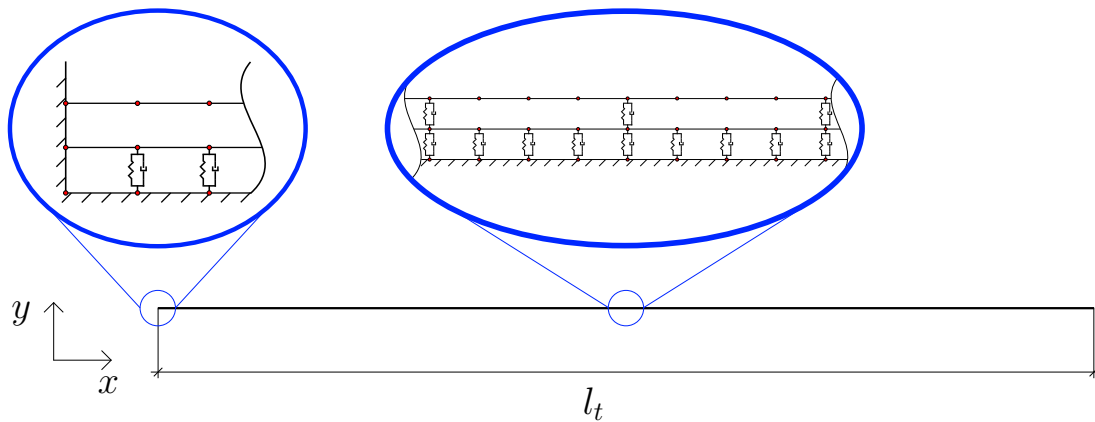


Figure 3.8: Sketch of the full Abaqus 2D model. Two parts are magnified; the far end illustrating the boundary conditions and the two middlemost rail seats showing the rail–panel connection. l_t is the full track length and the global coordinates, x and y are outlined.

3.2.2 Three-dimensional Slab Track Model

A number of concerns were raised in the development of the three-dimensional (3D) slab track model. To model and visualize geometrical features such as rail seats and to analyze the requested response, for instance panel bending moment and foundation reaction force in three spatial dimensions, the concrete panel is modeled using

solid elements. Implementing solid elements vastly increases the number of DOFs and thereby the computational power needed.

To construct a mesh that is adaptable, tetrahedral elements are used for the solid part. The specific element used is C3D10 which is a ten node tetrahedral element as illustrated in Figure 3.9. This element has four integration points, and the shape functions are presented in Zienkiewicz and Taylor [30]. For complex geometries, ABAQUS features an automatic mesh generator based on this kind of element. Consequent to the 2D model described in the previous section, the rail is modeled using R-T beam elements. However, for the 3D model each node has six DOFs and is in ABAQUS denoted B31.

The 3D model is constructed in several modules, each constituting one rail seat

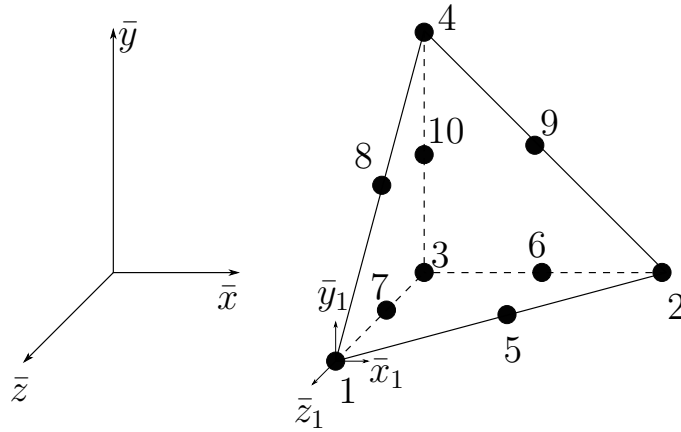


Figure 3.9: Sketch of a tetrahedral element with 10 nodes with local coordinates \bar{x} , \bar{y} and \bar{z} . Each node has three translational DOFs \bar{x}_i , \bar{y}_i and \bar{z}_i where i is the node number

distance, as seen in Figure 3.11(a). The module is periodically duplicated and coupled longitudinally to form the whole track model. The number of modules in the track structure is user defined, but the length has to be sufficient to attenuate boundary effects.

Each module is meshed individually, utilizing the fact that the module is symmetric in the longitudinal direction and thus a symmetric mesh is rendered. The user input defines the mesh density of the rail seats by one parameter, the mesh density of the panel body in lateral direction by one parameter, the mesh density in longitudinal direction of the panel body by one parameter and the mesh density in the vertical direction of the panel body by one parameter. The symmetric mesh

generation allows each module to be coupled in a node to node fashion. Figure 3.10 shows the edges of the 3D module that govern the mesh resolution.

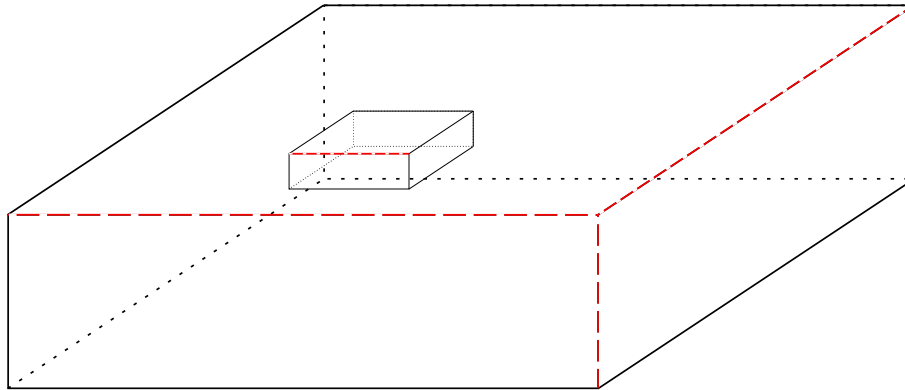


Figure 3.10: Sketch illustrating the edges arbitrating the mesh generation, which are indicated by the dashed lines in red. Input parameters decide the number of elements along each highlighted edge.

Each module is modeled with symmetry boundary conditions at the track center line, thereby representing only half of the actual track width, see Figure 3.11(b). At the rail seats, the DOFs of surface nodes are tied to the middle node of the rail seat surface (indicated by the node with cross hairs in Fig. 3.11(a)). This node is connected to one rail node at the same x - and z -coordinates. The rail pads are here represented by CONN3D2 elements which are identical to CONN2D2 elements with an additional option to include another translational DOF in the z -direction.

The Winkler foundation on the solid part of the concrete panel is represented by the ABAQUS feature SPRINGS/DASHPOTS TO GROUND. Since the nodes are uniformly and equidistantly distributed on the bottom panel surface, constant stiffness and damping values according to Table 3.1 can be used.

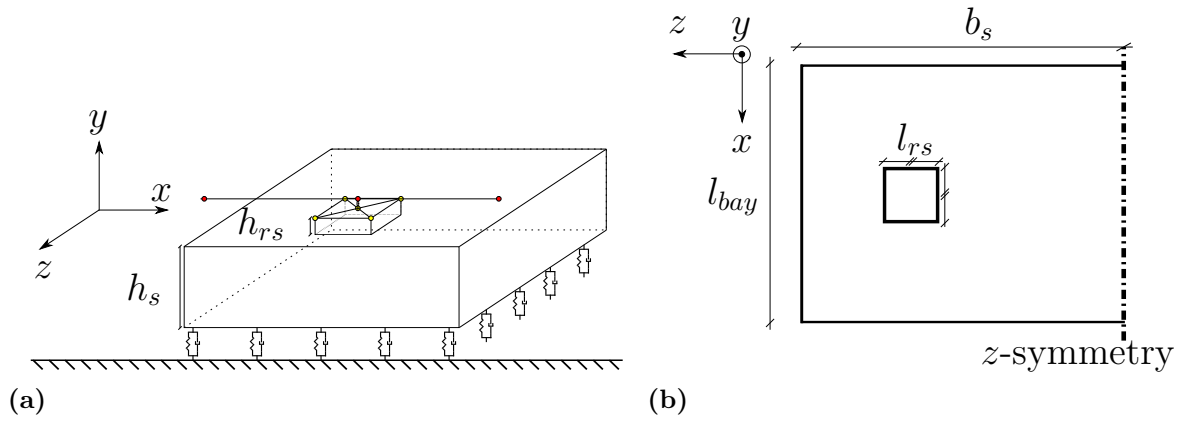


Figure 3.11: Magnified sketch of one rail seat module of the ABAQUS 3D slab track model, seen from the side (a) and from above (b). The rail and the slab are connected by a spring–dashpot pair at each rail tie connecting one rail node to all the surface nodes via the mid rail seat surface node indicated by the cross hairs on the rail seat. The slab is connected to the ground via spring–dashpot pairs with uniform stiffness and damping at each element node as a substitute for a Winkler foundation. Symmetry in the z -direction is applied in the middle of the track width. l_{bay} denotes the rail seat span length, l_{rs} is the length and width of the elevated portion of the rail seat, b_s is the concrete panel width, h_s is the concrete panel height and h_{rs} is the rail seat height. The global coordinate system is illustrated in both figures.

To connect each rail part, the ABAQUS feature COUPLING is used. The two end nodes of adjacent beam elements are merged into one node and thus share DOFs. The solid parts are connected in a similar way using the ABAQUS feature TIE. Rail elements of the whole track structure are modeled first in left to right order, allowing DOF numbering for the rail to be consequently ordered.

Since each module is symmetric in the longitudinal direction, the mesh patterns of the solid elements are identical on both sides which enables a node–node connection on the adjacent surfaces. Both these connections have been validated by conducting static computations on simple structures and load cases, see Figure 3.12.

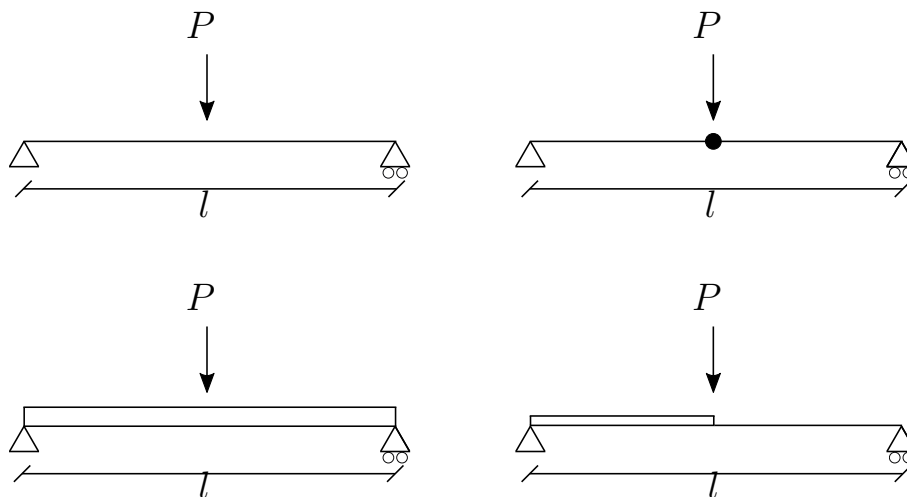


Figure 3.12: Sketch of different ABAQUS connection types that were verified by calculating the deflection after applying the same load P on structures with the same length l and having the same cross-sectional properties and mesh resolution. Upper left: beam with no connections. Upper right: beam to beam COUPLING connection. Lower left: Solid part with no connections. Lower right: Solid to beam MPC-beam connection.

A full track model of 120 rail seat distances with the concrete panel modeled using solid elements is computationally heavy. However, shortening the track is not an alternative due to the previously mentioned boundary reflections. The current work has adopted an alternative solution in which only the center most part of the concrete panel is modeled with solid elements, and the rest of the structure is modeled with beam elements (in this case B31 ABAQUS elements) in the same way as for the 2D model.

For such a design to provide adequate results, the connection between solid and beam elements must not render reflections that interfere with the results. Finally, it was decided to use a Multi-Point Constraint (MPC) connection in ABAQUS denoted MPC-beam, which ties the DOFs of the surface nodes of the solid elements to the DOFs of the first node of the beams representing the rest of the panel structure according to Figure 3.13. Practically, each node of the surface modeled with solid elements is connected through rigid beams, which enables moment to be transferred through the connection. This connection was validated according to Figure 3.12 and did not render any significant boundary effects in the results.

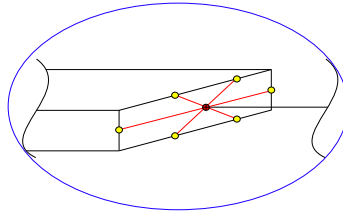


Figure 3.13: Sketch of the MPC connection between the solid and beam element parts of the slab. The yellow nodes represent the surface nodes on the solid element, whose DOFs are all tied to the DOFs of the adjacent beam node (the red node with cross hairs).

The 3D model used for the simulations in Chapter 4 has 120 rail seat distances and a total length of 78 m. The concrete panel on a user defined number of middlemost rail seats are solid elements and the rest of the structure is modeled analogous to the 2D model. The ends of both rail and concrete panel are fixed. See Fig. 3.14 for an illustration of the whole structure.

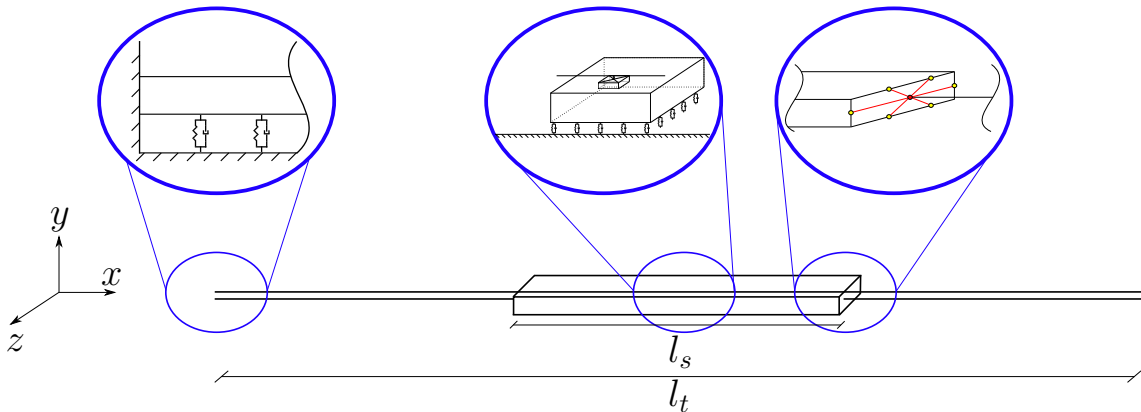


Figure 3.14: Sketch of the whole 3D ABAQUS track model. Three sections of the model are magnified. The far end, a rail seat distance modelled with solid elements and the MPC connection between solid and beam elements. l_s denotes the length of the solid part of the track and l_t is the total length of the track. The global x , y and z coordinates are outlined.

3.3 Simulation Phase

The properties of the generated track structures, in the form of node and element topology and global system matrices \mathbf{K} , \mathbf{M} and \mathbf{C} are exported to Matlab. In Matlab, topology information is used to sort the system matrices for the subsequent static and dynamic calculations. The simulation phase is summarized in Fig. 3.15.

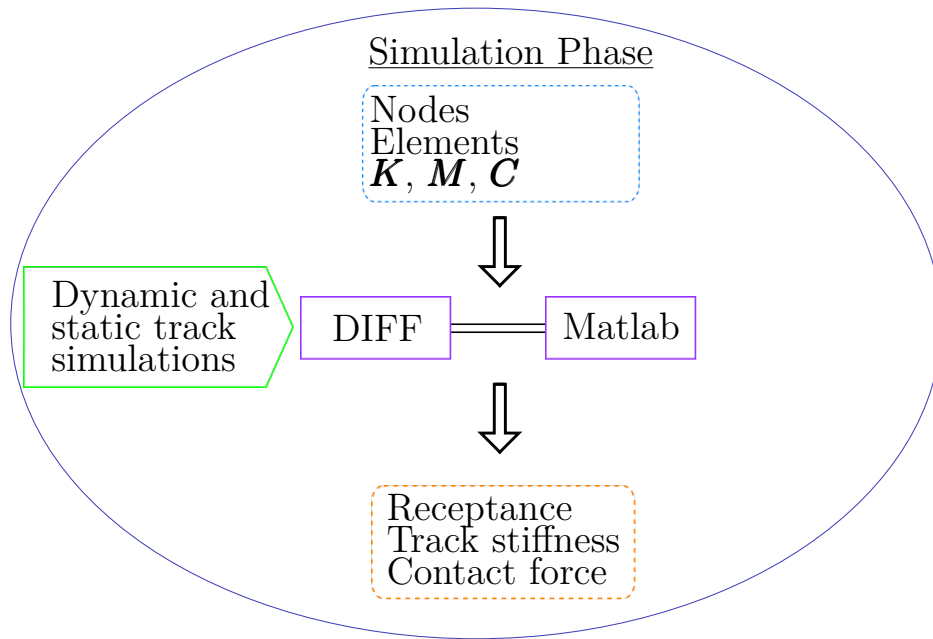


Figure 3.15: In the simulation phase, the node and element information is used to sort the global system matrices exported to Matlab and subsequently used in the simulations. The simulation results include receptance, track stiffness at the rail level and wheel–rail contact forces calculated in the software DIFF.

3.3.1 Non-moving Load Problem

The response of the track to a non-moving load was investigated. The track response in the frequency domain is analyzed by calculating the receptance at different positions of the track. The receptance is given as

$$\underline{H}(\omega) = \frac{\underline{u}}{\underline{F}} \quad (3.2)$$

where \underline{u} is a displacement at a given DOF in the track model and \underline{F} is the force applied at any DOF along the rail. $\underline{\mathbf{u}}$ (a vector containing all DOFs) is calculated in the frequency domain as

$$\underline{\mathbf{u}}(\omega) = \frac{\underline{\mathbf{F}}}{\underline{\mathbf{K}} + i\omega\underline{\mathbf{C}} - \omega^2\underline{\mathbf{M}}} \quad (3.3)$$

where $\underline{\mathbf{F}}$ is the load vector. To get the receptance at a single DOF (as in Equation (3.2)), the DOF of interest is extracted from $\underline{\mathbf{u}}$. The static track response is represented by the track stiffness at the rail level and is taken as of $\underline{H}(\omega = 0)^{-1}$ at any longitudinal coordinate along the rail.

3.3.2 Dynamic simulations in DIFF

DIFF is an in-house software developed by Nielsen and Igeland [12] and stands for Dynamisk Interaktion mellan Fordon och Farbana (Dynamic Interaction between Vehicle and Track). DIFF is implemented in Matlab and utilizes the modal superposition technique and time integration procedure covered in Section 2.3.2. DIFF has previously been validated by comparing simulation results to experimental data for ballasted tracks. In the current work simulations in DIFF are performed to calculate wheel–rail contact forces, which are solved from the initial value problem in Eq. (2.40) and included in $\underline{\dot{z}}$.

The vehicle used for the dynamic simulations consists of one bogie with two wheelsets as seen in Figure 2.6. The bogie is modeled by six DOFs, and contains two unsprung masses M_{b1} and M_{b2} separated by the distance l_b and a bogie frame with the mass M_{b3} . Also, the bogie is influenced by the mass of the car body M_0 and the total axle load is 17 tonnes. The parameter values for the vehicle are taken from [31] and displayed in Table 3.2.

Table 3.2: Parameter values for the vehicle model used in the dynamic simulations, taken from Iwnicki [31].

Parameter	Value	Legend
M_{b1}	1.8 tonnes	Mass of the first wheelset
M_{b2}	1.8 tonnes	Mass of the second wheelset
M_{b3}	2.6 tonnes	Mass of the bogie frame
M_0	28 tonnes	Mass of the car body
J_{b3}	1476 kgm ²	Bogie frame inertia
l_b	2.6 m	Bogie length
k	1.2 MN/m	Wheelset suspension stiffness
c	4 kNs/m	Wheelset suspension damping
C_H	93 GN/m ^{3/2}	Hertzian contact coefficient

4

Numerical Results

In the following chapter, the numerical results are presented. In Section 4.1, the method is validated by comparing results between the two-dimensional (2D) model developed by Aggestam et al. [27] (DIFF model) and the developed 2D ABAQUS model. The results from the developed 3D ABAQUS model are presented in Section 4.2.

4.1 Verification of Modeling Procedure

To verify the procedure presented in Chapter 3, the numerical results of the 2D model developed in ABAQUS are compared to those calculated with the DIFF model. Throughout this chapter, the relative error is computed according to

$$\eta = \frac{|v^{\text{DIFF}} - v^{\text{ABAQUS}}|}{v^{\text{DIFF}}}, \quad (4.1)$$

where v^{DIFF} and v^{ABAQUS} are computed values (receptance, track stiffness or wheel-rail contact force) for the DIFF and ABAQUS models, respectively.

4.1.1 Receptance

Receptances of the proposed and existing models are compared. A vertical harmonic load (in the frequency range 0–1500 Hz) is applied at the mid rail seat (rail seat 61 out of 121). The response, given by the deflection per unit force, can be calculated at any DOF in the system. In Figure 4.1(a), the direct receptance (response is calculated at the same DOF as the excitation) is presented. Also, the relative error of the receptance calculated with both models is presented in Figure 4.1(b). Figure 4.2 presents the amplitude (a) and relative error (b) of the cross receptance calculated at the slab for excitation at the mid rail seat, respectively. The displacement of the slab is taken at the same longitudinal coordinate as the rail excitation.

4. Numerical Results

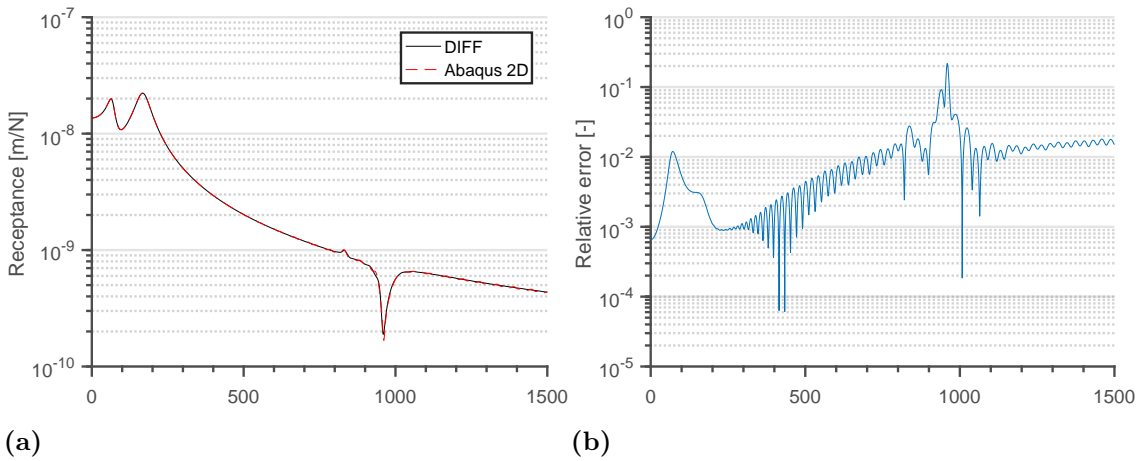


Figure 4.1: Magnitude (a) and relative error (b) of the direct receptance calculated for the 2D ABAQUS model and the DIFF model. The excitation and response are taken at the middle rail seat.

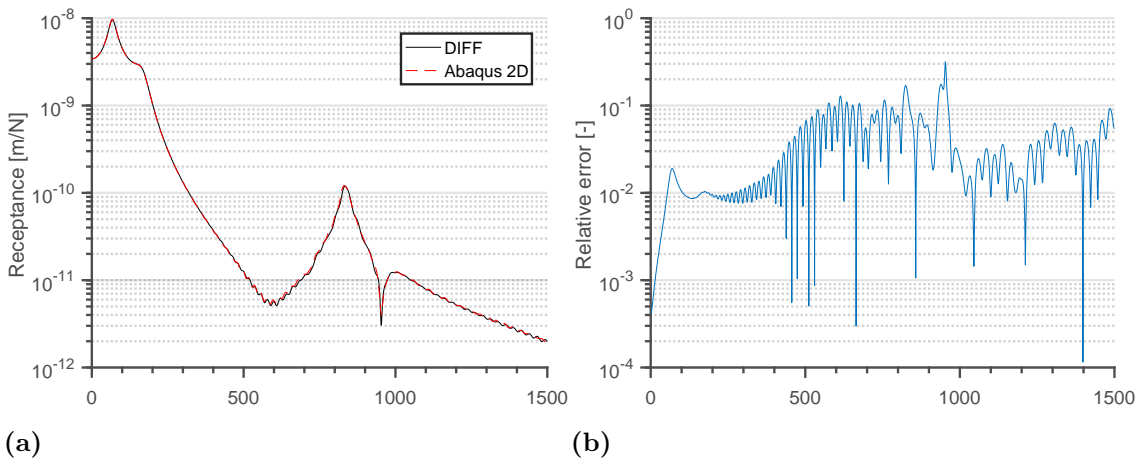


Figure 4.2: Magnitude (a) and relative error (b) of the cross receptance calculated for the ABAQUS 2D model and the DIFF model. The excitation and response are taken at the longitudinal coordinate corresponding to the mid rail seat at the rail and slab, respectively.

In Figure 4.1(a), two resonances and one anti-resonance are noted. At the first resonance frequency at about 100 Hz, the slab and rail move in phase which is indicated by that the same resonance can be seen in Figure 4.2(a). At the second resonance frequency at about 200 Hz, the slab and rail move out of phase. The anti-resonance at about 950 Hz represents the so-called pinned–pinned eigenmode. At this mode, the rail vibrates with a wavelength corresponding to two rail seat distances [12]. It is also noted that the resonance at about 850 Hz in Figure 4.2(a) can be seen as a small peak in Figure 4.1(a). Figures 4.1 and 4.2 show that the receptance of the two

models are in good agreement. The largest deviation is found at the pinned-pinned mode.

4.1.2 Track Stiffness at the Rail Level

Based on the stiffness matrices of the track models, the static track stiffness at the rail level is investigated, see Figure 4.3. The periodic pattern in Figure 4.3(a) is a result of the discrete rail supports where each peak represents a rail support. It is clear from Figure 4.3(b) that the results from the two models are in good agreement.

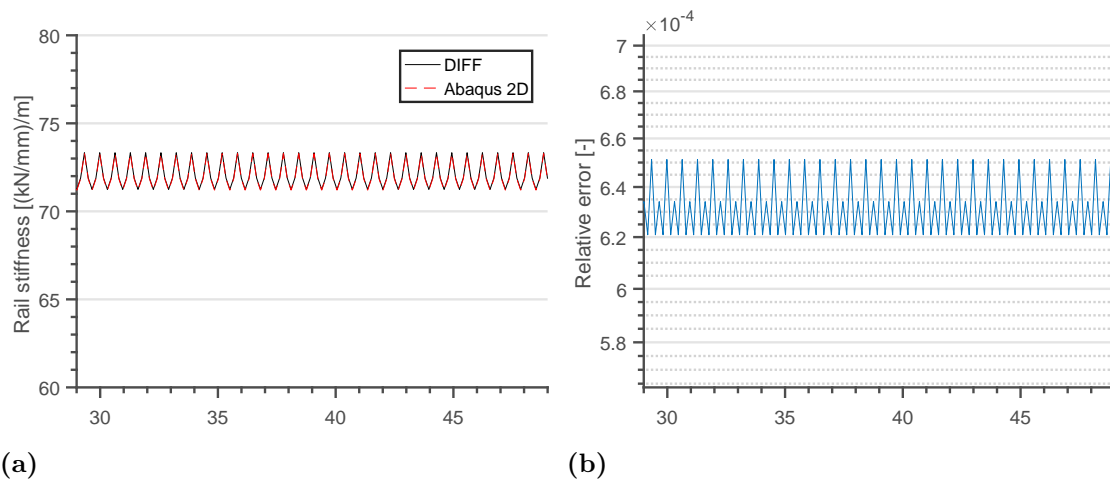


Figure 4.3: Magnitude (a) and relative error (b) of the slab track stiffness at the rail level calculated for the 2D ABAQUS model and the previously developed DIFF model.

4.1.3 Vertical Wheel–Rail Contact Force

Simulations of vertical dynamic vehicle–track interaction are performed. Figures 4.4 and 4.5 present wheel–rail contact forces calculated without or with broadband irregularities modeled on the running surface of the rail, respectively.

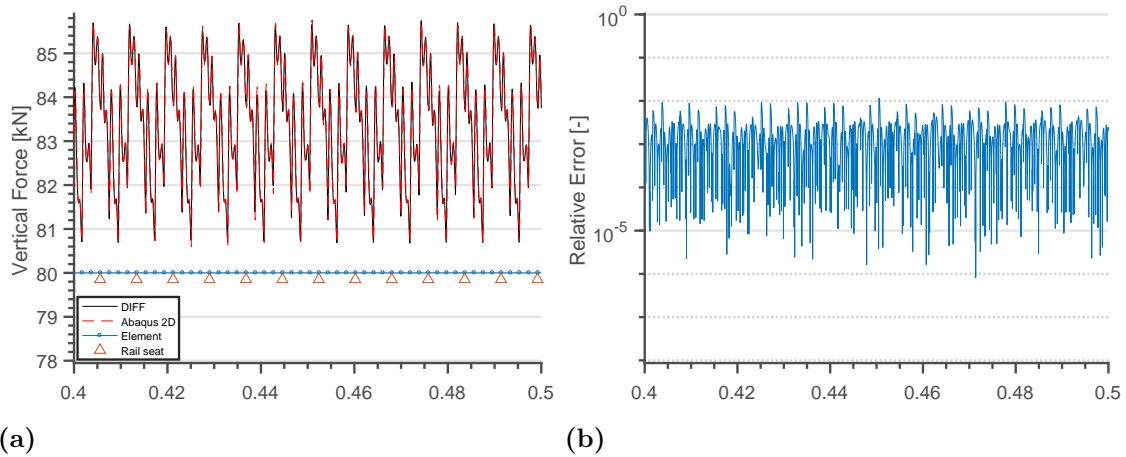


Figure 4.4: Magnitude (a) and relative error (b) of vertical wheel–rail contact force simulated using the ABAQUS 2D model and the previously developed DIFF model. Time step 10^{-5} s. Locations of rail seats and nodes of beam elements in the rail FE model are outlined.

As seen in Figure 4.4, the contact forces show the same periodic pattern as the track stiffness presented in Figure 4.3. This is a direct consequence of the periodic excitation caused by the discrete rail seats. In addition, excitation at the element passing frequency is observed. This is due to the discontinuity in slope of the interpolation polynomials from R–T beam theory, which are presented in Equation (2.9). These disturbances, which would not have been present if E–B beam theory was used, can be filtered out using a low-pass filter.

The vertical dynamic vehicle–track interaction is further investigated by introducing an irregularity with wavelengths in the range 2 cm–10 m and amplitudes according to the limit in ISO3095 [32]. The irregularity is added to the vector \mathbf{x}^{irr} in Equation (2.31). The calculated vertical wheel–rail contact force is presented in Figure 4.5.

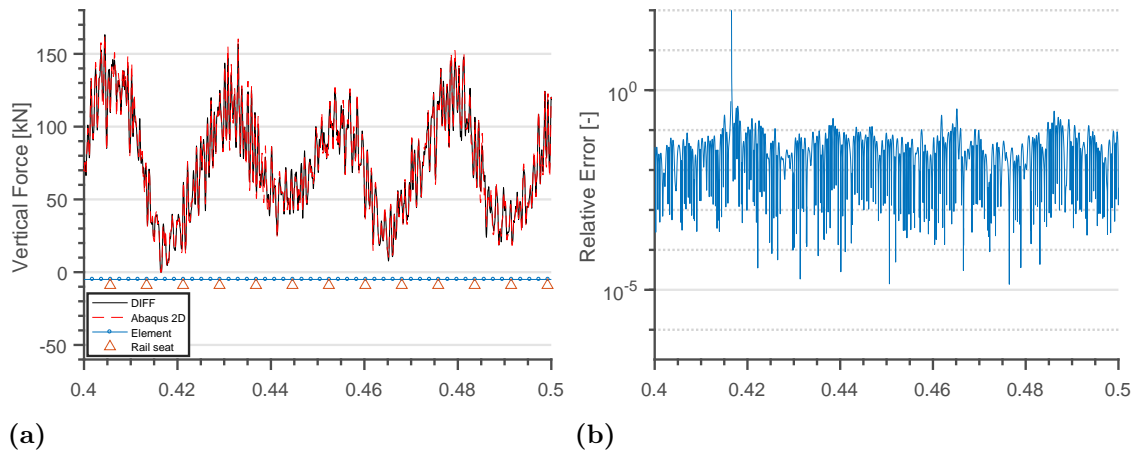


Figure 4.5: Magnitude (a) and relative error (b) of vertical wheel–rail contact force simulated using the ABAQUS 2D model and the previously developed DIFF model. Broadband irregularities with wavelengths in the range 2 cm – 100 cm and amplitudes taken as the limit in ISO3095 [32] is modeled on the rail. Locations of rail seats and nodes of beam elements in the rail FE model are outlined.

In Figure 4.6, the spectrum of the vertical contact force simulated for the ABAQUS 2D model is compared with the previously developed DIFF model. The results show good agreement. The peak in relative error at about 0.415 s seen in Figure 4.5, is explained by a loss of wheel–rail contact.

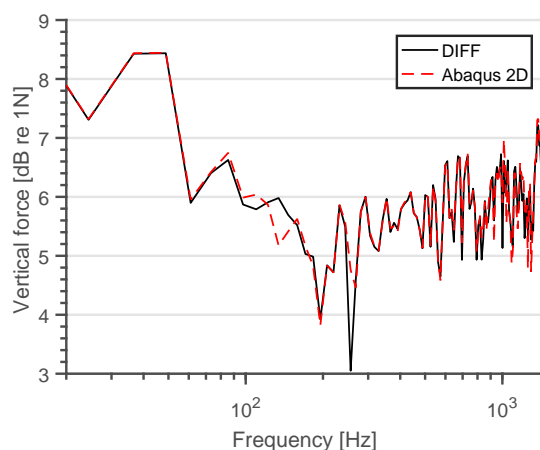


Figure 4.6: Spectrum of the vertical wheel–rail contact force calculated for the ABAQUS 2D model and the DIFF model. Broadband irregularities with wavelengths in the range 2 cm – 100 cm and amplitudes taken as the limit in ISO3095 [32] is modeled on the rail.

4.2 Three-dimensional Slab Track

Results simulated for the 3D ABAQUS model are presented in the following section. Again, the DIFF model is used for comparing the numerical results. The results give an indication if the assumptions for the 2D model are valid, it also offers an opportunity to fine-tune the DIFF model according to a more detailed 3D model in future work.

4.2.1 Receptance

Analogous to the ABAQUS 2D model, the frequency response of the 3D model is investigated by calculating the receptance. The load is applied on the rail at the middle rail seat. For the direct receptance the response is calculated at the same DOF, see Figure 4.7. Figure 4.7 shows no sign of significant boundary reflections originating from e.g. the transition between track sections modeled with solid and beam elements.

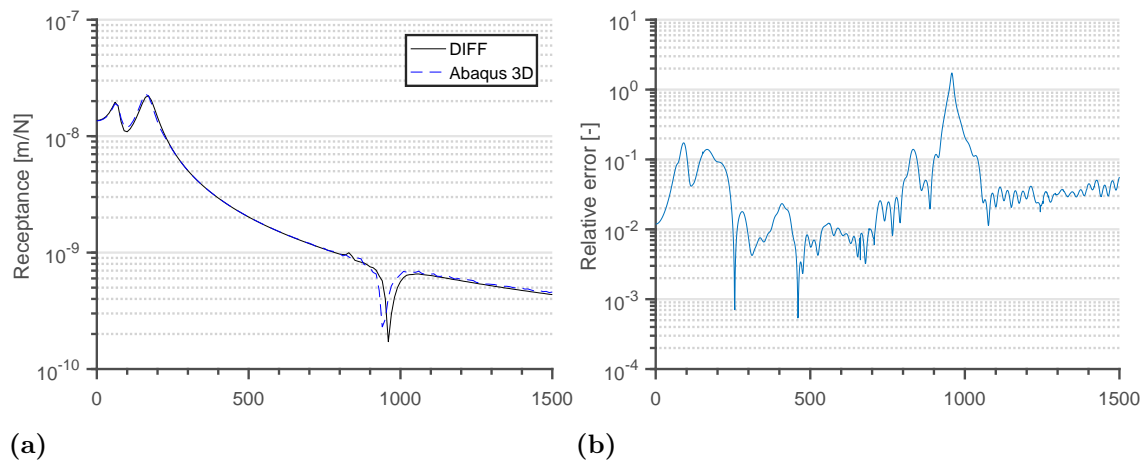


Figure 4.7: Magnitude (a) and relative error (b) of the direct receptance calculated for the 3D ABAQUS model and the DIFF model. The excitation and response are taken at the middle rail seat.

4.2.2 Track Stiffness at the Rail Level

The track stiffness at the rail level of the 3D model compared to the 2D DIFF model is presented in Figure 4.8. From Figure 4.8, it is apparent that the part of the track modeled with solid elements has a marginally higher stiffness than the rest of the track structure. This effect can be further investigated conducting parametric studies by changing for example the foundation stiffness.

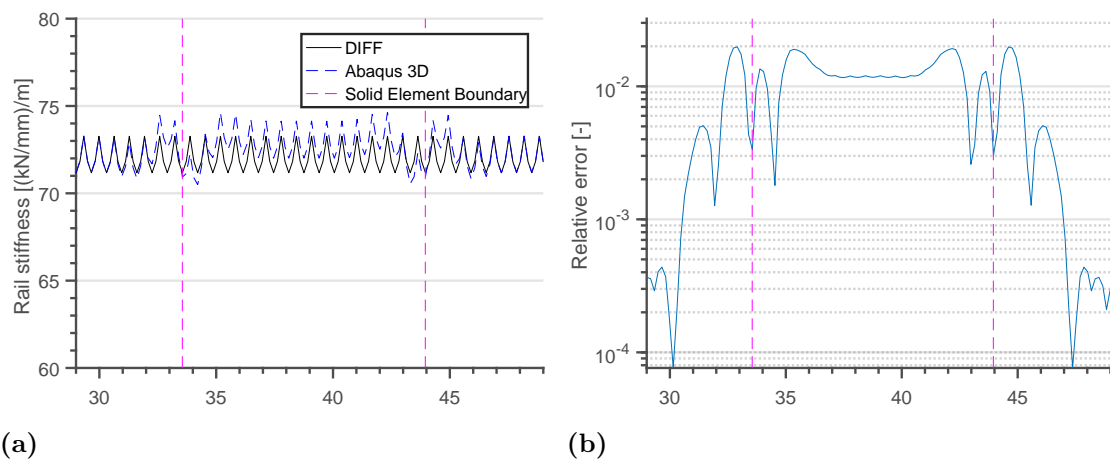


Figure 4.8: Magnitude (a) and relative error (b) of the static slab track stiffness calculated for the 3D ABAQUS model and the previously developed DIFF model. The boundaries between sections of the concrete panel modeled with solid and beam elements are outlined by vertical lines.

4.2.3 Vertical Wheel–Rail Contact Force

Figure 4.9 presents the vertical wheel–rail contact force calculated without rail irregularities. Figure 4.9 shows the difference in stiffness between the solid and the beam part of the track to render disturbances in the wheel–rail contact force. This disturbance is stabilized under the course of the simulation, until the bogie reaches the other boundary, where the disturbances are introduced again, see Figure 4.9(b). Hence, the part of the track modeled with solid elements must be of sufficient length to produce reliable results. A closer look at the time span between 0.5 s and 0.6 s is presented in Figure 4.10. Figure 4.10 shows that the contact force, when stabilized, show close agreement compared to the simulations run on the 2D DIFF model.

4. Numerical Results

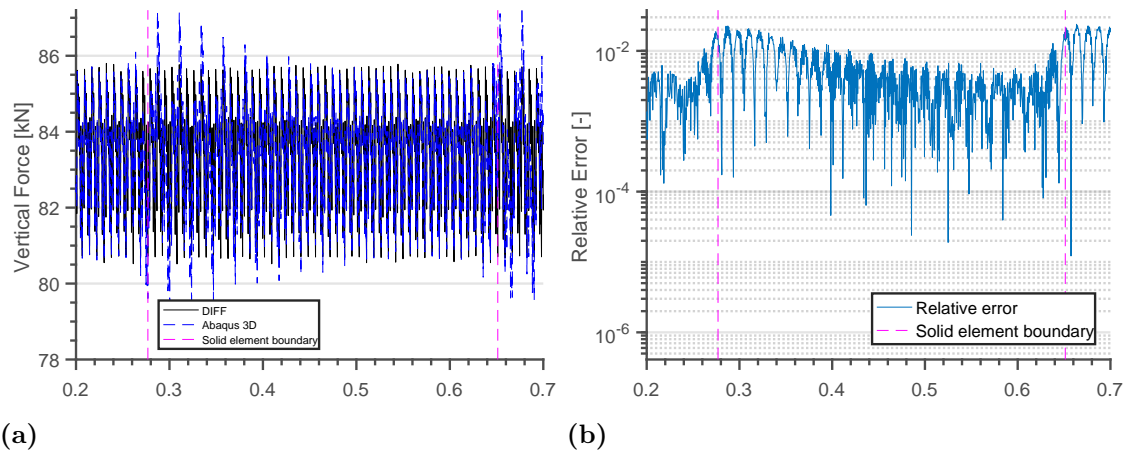


Figure 4.9: Magnitude (a) and relative error (b) of vertical wheel–rail contact force simulated using the ABAQUS 3D model and the previously developed DIFF model. Time step 10^{-5} s. The boundaries between sections of the concrete panel modeled with solid and beam elements are outlined by vertical lines.

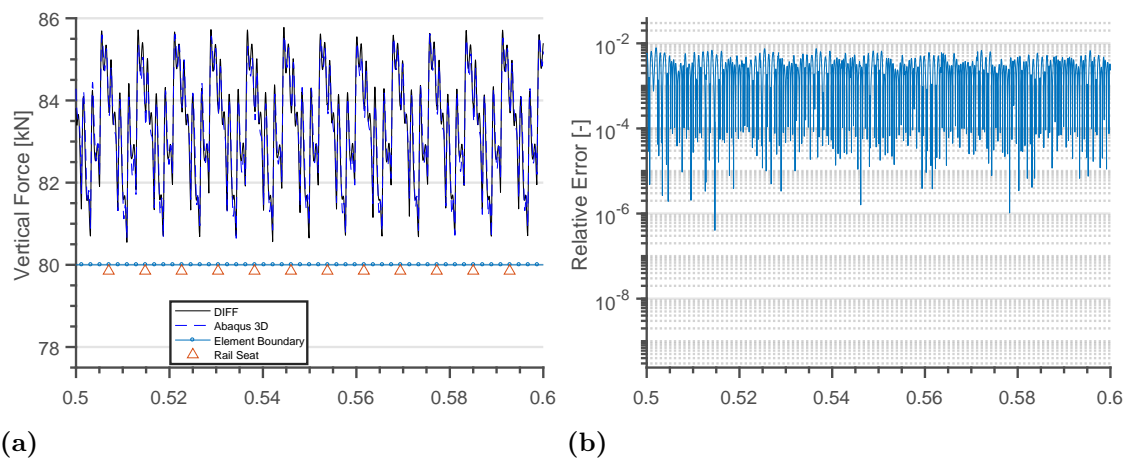


Figure 4.10: Magnitude (a) and relative error (b) of vertical wheel–rail contact force simulated using the ABAQUS 3D model and the previously developed DIFF model. Time step 10^{-5} s. Locations of the rail seats and element boundaries are outlined.

Furthermore, the irregularity from ISO3095 is introduced on the rail and the results are presented in Figure 4.11. In Figure 4.12, the spectrum of vertical wheel–rail contact force simulated for the ABAQUS 3D model and the previously developed DIFF model are compared.

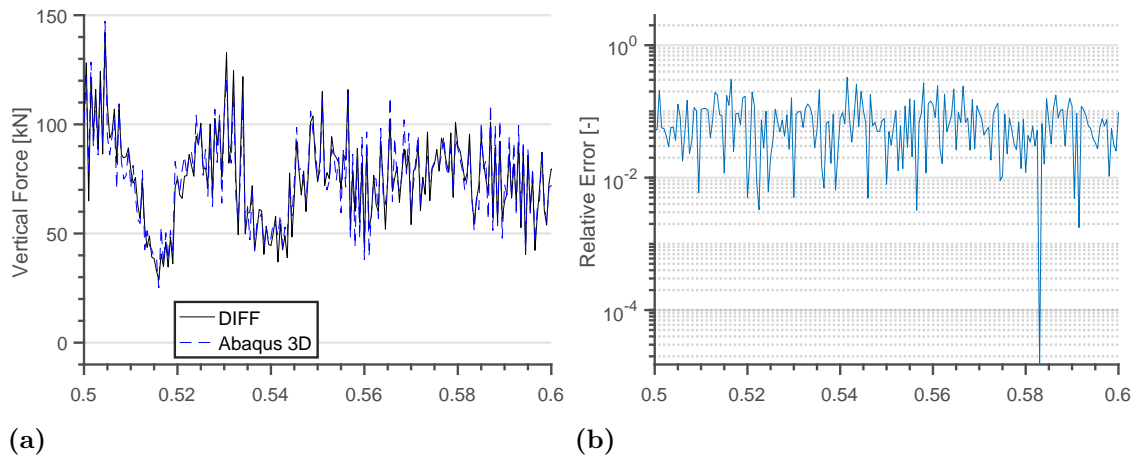


Figure 4.11: Magnitude (a) and relative error (b) of vertical wheel–rail contact force simulated using the ABAQUS 3D model and the previously developed DIFF model. Broadband irregularity with wavelengths in the range 2 cm – 100 cm and amplitudes taken as the limit in ISO3095 [32] is modeled on the rail.

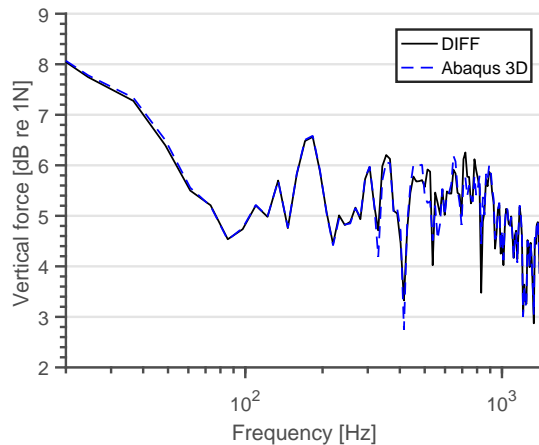


Figure 4.12: Spectrum of the vertical wheel–rail contact force calculated for the ABAQUS 3D model and the DIFF model. Broadband irregularities with wavelengths in the range 2 cm – 100 cm and amplitudes taken as the limit in ISO3095 [32] is modeled on the rail.

Finally, simulations of wheel–rail contact force with rail irregularities based on ISO3095 comparing the mesh density of the the track section modeled with solid elements are conducted, see Figure 4.13. Three mesh densities are compared, low (532 nodes per rail seat distance), medium (1374 nodes per rail seat distance) and high (2284 nodes per rail seat distance). Figure 4.13 indicates that at the rail level, simulation results are not influenced to a large extent by the mesh resolution of the solid elements in the concrete panel.

4. Numerical Results

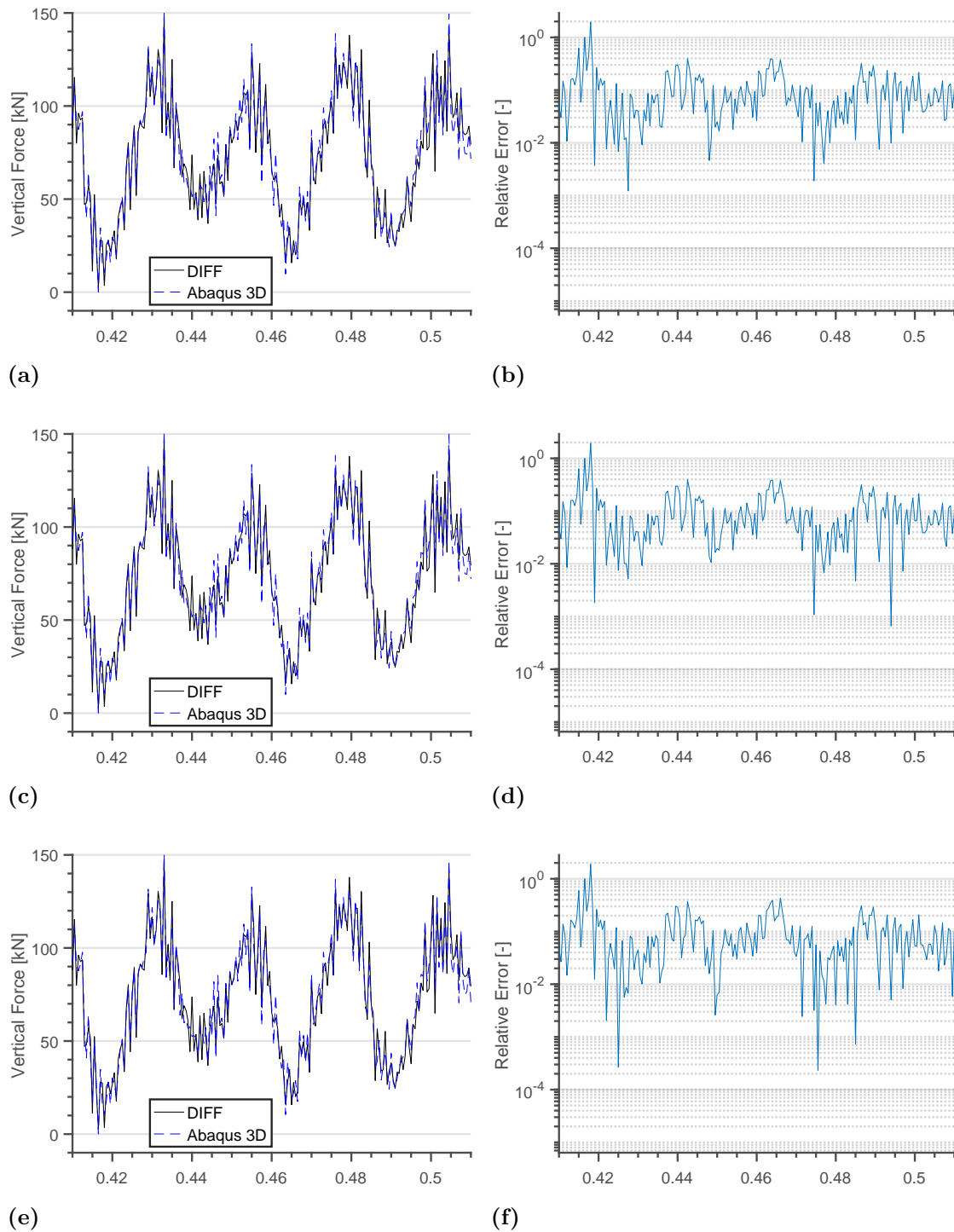


Figure 4.13: Magnitude (a, c, e) and relative error (b, d, f) of vertical wheel–rail contact force simulated using the ABAQUS 3D model and the previously developed DIFF model. Broadband irregularity with wavelengths in the range 2 cm – 100 cm and amplitudes taken as the limit in ISO3095 [32] is modeled on the rail. Simulations conducted on 3D models with low mesh resolution (a–b), medium mesh resolution (c–d) and high mesh resolution (e–f).

5

Summary and Conclusions

A methodology to introduce finite element (FE) slab track models implemented in the commercial software ABAQUS into an existing in-house software for simulation of dynamic vehicle–track interaction (DIFF) has been developed. The procedure is validated by comparison of track receptance, track stiffness at the rail level and dynamic wheel–rail contact forces simulated for a two-dimensional (2D) slab track model built in ABAQUS towards those obtained with an existing model.

In ABAQUS, the track models are generated by Python scripts interpreted in the application programming interface (API). The geometry of the slab track (e.g. model length, design of concrete panel and distance between rail seats) as well as properties of the numerical approximation (e.g. density of FE mesh and number of eigenmodes included in the modal reduction) are parameterized in order to allow for parametric studies.

The 2D slab track model used for validation consists of two ABAQUS elements; B21 Rayleigh–Timoshenko (R–T) beam elements to model the rail and concrete panel, and CONN2D2 connector elements to model rail pads and soil. The subsequently developed 3D model includes B31 and CONN2D3 elements (the three dimensional equivalents to the elements of the 2D model), and in addition the C10D3 solid element. To reduce the number of DOFs, only a central portion of the concrete panel is modeled with solid elements whereas the surrounding parts are modeled with R–T beam elements. Boundaries between the concrete panel modeled with R–T and C10D3 elements are connected using Multi-Point-Constraints (MPC) which introduces a rigid connection between the surface nodes of the concrete panel modeled with solid elements and the adjacent node of the part modeled with beam elements.

Simulations of vertical dynamic vehicle–track interaction are performed using the in-house software DIFF. A high-speed vehicle consisting of one bogie is modeled. In DIFF, the moving load problem of a railway vehicle traversing a slab track is

solved by numerical time-integration using an extended state-space vector approach in combination with a complex-valued modal superposition technique.

The vertical wheel–rail contact force simulated for the three-dimensional (3D) slab track model shows disturbances originating from the entrance of the concrete panel modeled with solid elements. This puts requirements on the minimum length of this part of the concrete panel in order for the contact force to stabilize. The associated excitation is likely due to the slight difference in track stiffness experienced by the wheel as it moves from the part of the track where the slab is modeled with beam elements to that modeled with solid elements.

The vertical direct rail receptance calculated for the 3D slab track model shows a slight deviation in frequency for the pinned-pinned eigenmode compared to that obtained for the 2D model. Comparison of the vertical wheel–rail contact force simulated for the 2D and 3D slab track model shows a good agreement. For the same length of the track model, simulations with the 3D slab track model is about a factor 2 times more time consuming compared to the 2D slab track model. This is due to the increased number of DOFs (also after modal reduction since eigenmodes up to the same maximum eigenfrequency are used) of the 3D model. In the current work eigenmodes corresponding to eigenfrequencies up to approximately 1500 Hz are accounted for in both track models.

6

Further Work

In the PhD project CHARMEC TS19, design criteria for future slab track structures are to be defined. In the current work, the simulation methodology including a three-dimensional (3D) slab track model has been developed and can be used in further work involving vehicle-track interaction. In the following paragraphs, model refinements and proposed changes are discussed.

The geometry and properties of the concrete panel can be calibrated in order to in a larger extent resemble a real life track design. Rail seats and rail pads can be altered and reinforcement bars can be included in the model. To validate the method, data measured on an experimental test rig or in the field is required. In particular, dynamic vertical wheel-rail contact force measured with for example an instrumented wheelset would be useful. This way, the developed model can be tuned with respect to real life experimental data. Parametric studies to test modeling assumptions such as foundation stiffness distribution, rail pad stiffness, etc. are also suggested.

A further development of the post-processing to enable the calculation of bending moment in the concrete panels and force distribution on the foundation is proposed. Analyzing the moment distribution in three dimensions allows for criteria to be set concerning concrete strength, reinforcement density, crack propagation allowance etc. Analyzing the foundation force distribution is of great importance since setting the requirements for the foundation relies on the allowed settlements, which has a big influence in the amount of ground improvement needed before construction and thus the investment cost for future railways built with slab track technology.

Bibliography

- [1] Trafikverket, “En ny generation järnväg - höghastighetsjärnväg i Sverige,” <https://www.trafikverket.se/resa-och-trafik/jarnvag/nygenerationjarnvag>, 2017, accessed: 2017-10-27.
- [2] W. Zhai, K. Wang, and C. Cai, “Fundamentals of vehicle-track coupled dynamics,” *Vehicle System Dynamics*, vol. 47, no. 11, pp. 1349–1376, 2009.
- [3] C. Esveld, “Recent developments in high-speed track,” *European Railway Review*, vol. 9, pp. 81–86, 2003.
- [4] UIC High Speed Department, “Origin and financing of first high-speed lines in the world,” 2014, International Union of Railways.
- [5] L. Lennefors, “Nya stambanor i plan 2018–2029. utbyggnadsstrategi för höghastighetsjärnvägar. underlagsrapport till nationell plan för transportsystemet 2018–2029,” Trafikverket, Borlänge, Tech. Rep. 2017:168, Augusti 2017.
- [6] J. Zwolski, “Lectures 1, 5 and 9,” Wrocław, 2013, Wrocław: Wrocław University of Technology. Lecture slides.
- [7] P.-E. Gautier, “Slab track: Review of existing systems and optimization potentials including very high speed,” *Construction and Building Materials*, vol. 92, pp. 9–15, 2015.
- [8] Max-Bögl, “FFB slab track Bögl,” Sengenthal, Germany.
- [9] J. W. Schwedler, “Discussion on iron permanent way,” *Wood, Charles: Iron Permanent way. Minutes of Proc. of the Instn of Civ. Engrns, London*, vol. 67, pp. 95–118, 1882.
- [10] K. Knothe and S. L. Grassie, “Modelling of railway track and vehicle/track interaction at high frequencies,” *Vehicle System Dynamics*, vol. 22, no. 3-4, pp. 209–262, 1990.
- [11] Y.-H. Lin and M. W. Trethewey, “Finite element analysis of elastic beams

- subjected to moving dynamic loads,” *Journal of Sound and Vibration*, vol. 136, no. 2, pp. 212–231, 1990.
- [12] J. C. O. Nielsen and A. Igeland, “Vertical dynamic interaction between train and track - influence of wheel and track imperfections,” *Journal of Sound and Vibration*, vol. 187, no. 5, pp. 825–839, 1995.
- [13] M. Enelund, “Continuous Beams,” 2015, Göteborg: Chalmers University of Technology. Lecture slides 17-19 in TME141 Structural Dynamics.
- [14] W. Scholl, “Darstellung des Körperschalls in Platten durch Übertragungsmatrizen und anwendung auf die Berechnung der Schwingungsformen von Eisenbahnschienen,” *Fortschritt- Berichte VDI*, vol. 11, no. 93, 1987, Düsseldorf: VDI-Verlag.
- [15] A. Haque, “An introduction to the Timoshenko beam element,” 2016, unpublished paper.
- [16] H. Benorya and M. Nagurka, *Mechanical Vibration - Analysis, Uncertainties and Control*. Boca Raton, Florida: CRC Press LLC, 2009, third Edition.
- [17] S. Timoshenko, W. Weaver, and D. Young, *Vibration Problems in Engineering*. New York: Wiley & Sons, 1990.
- [18] J. H. Sällström, “Fluid-conveying damped Rayleigh–Timoshenko beams in transverse vibration analyzed by use of an exact finite element part ii: Applications,” *Journal of Fluids and Structures*, vol. 4, no. 6, pp. 573–582, 1990.
- [19] S. Chandra, “Modelling of soil behavior,” Kanpur, 2014, Kanpur: Indian Institute of Technology Kanpur. Lecture slides.
- [20] A. Johansson and J. C. O. Nielsen, “Out-of-round railway wheels—a literature survey,” *ImechE Journal of Rail and Rapid Transit*, vol. 214, no. F2, pp. 79–91, 2000.
- [21] A. Ekberg and H. Bjarnehed, *Rolling contact fatigue of wheel/rail systems—a literature survey*. Gothenburg: Chalmers Solid Mechanics, 1995.
- [22] S. L. Grassie and J. Kalousek, “Rail corrugation: Characteristics, causes and treatments,” *ImechE Journal of Rail and Rapid Transit*, vol. 223, pp. 581–596, 1993.
- [23] X. Zhu, “Tutorial on Hertz contact stress,” 2012, Tucson, Arizona: The Uni-

-
- versity of Arizona. Handout in OPTI 421/521 Introductory Optomechanical Engineering.
- [24] E. Andersson, M. Berg, and S. Stichel, *Rail Vehicle Dynamics*. Stockholm: Kungliga Tekniska Högskolan, 2014.
- [25] K. L. Johnson, *Contact Mechanics*. Cambridge: Cambridge University Press, 1985.
- [26] J. A. Greenwood and J. H. Tripp, “The elastic contact of rough spheres,” *Journal of Applied Mechanics*, vol. 34, pp. 153–159, 1967.
- [27] E. Aggestam, J. C. O. Nielsen, and R. Bolmsvik, “Simulation of vertical dynamic vehicle–track interaction using a two-dimensional slab track model,” *Vehicle System Dynamics*, 2018.
- [28] Dassault Systèmes Simulia, “ABAQUS unified FEA,” <https://www.3ds.com/products-services/simulia/products/abaqus/>, accessed: 2018-01-07.
- [29] Dassault Systèmes Simulia, “ABAQUS 6.14 Online Documentation - Theory Guide - 3.5.2 Beam Element Formulation,” <http://abaqus.software.polimi.it/v6.14/books/stm/default.htm?startat=ch03s05ath74.html>, 2014, accessed: 2017-10-25.
- [30] O. C. Zienkiewicz and R. L. Taylor, *The Finite Element Method—Volume 1: The Basis*. Oxford: Butterworth-Heinemann, 2000, fifth Edition.
- [31] S. Iwnicki, “Manchester benchmarks for rail vehicle simulation,” *Vehicle System Dynamics*, vol. 30, no. 3-4, pp. 295–313, 1998.
- [32] The International Organization for Standardization (ISO), “ISO 3095:2013(en),” <https://www.iso.org/obp/ui/#iso:std:iso:3095:ed-3:v1:en>, 2013, accessed: 2017-11-21.

